

**ACTIVE SOURCE 3D SEISMIC TOMOGRAPHY OF BRADY
HOT SPRINGS GEOTHERMAL FIELD, NEVADA**

by

Lesley Parker

A thesis submitted in partial fulfillment of the requirements for

the degree of

Master of Science

(Geophysics)

at the

UNIVERSITY OF WISCONSIN-MADISON

2017

Acknowledgements

ORMAT Technologies generously provided access to the site and cooperated with the entire PoroTomo Project. We thank Fan-Chi Lin, Amanda Thomas, and Marianne Karplus for loaning nodal instruments, Jamie Farrell for assistance with the nodal data, and IRIS-PASSCAL for loaning Refteks and sensors. The Geothermal Technologies Office of the U.S. Department of Energy supported this research through grant DE-EE0006760. The data used can be found on the Geothermal Data Repository at <http://gdr.openei.org/>, keyword: PoroTomo.

I would like to thank my advisor Cliff Thurber; your expertise and guidance were invaluable. In addition, I would like to thank Dante Fratta and Harold Tobin for serving on my committee.

None of this could have been done without the entire PoroTomo team. Kurt Feigl, Christina Morency, Doug Miller, Elena Reinisch, Herb Wang, Janice Lopeman, Jeremy Patterson, Joe Greer, John Akerley, Eric Matzel, Mike Cardiff, Michelle Robertson, Neal Lord, Rob Mellors, Tabrez Ali, Thomas Coleman, Whitney Trainor-Guitton, Bill Foxall, and Chelsea Lancelle. I'd particularly like to thank Xiangfang Zeng and Peng Li for helping me with my coding and answering my many questions.

Additionally, thank you to Bin Guo for the use of his autopicker and to my other officemates, Sarah Bremmer and Crystal Wespestad, for their support and companionship. Thank you to Beatriz Cosenza, Stephanie Napieralski, Elisabeth Schlaud, Reagan Cronin, Federica Lanza, and my other fellow grad students for your advice and for reminding me to get out of my office on occasion. Finally, Michael Parker, thank you for your support, understanding, and patience.

Abstract

We deployed a dense seismic array to image the shallow structure in the injection area of the Brady Hot Springs geothermal site in Nevada. The array was composed of 238 5 Hz, three-component nodal instruments and 8,700 m of distributed acoustic sensing (DAS) fiber-optic cable installed in surface trenches plus 400 m installed in a borehole. The geophone array had about 60 m instrument spacing in the target zone, whereas DAS channel separations were about 1 m. The acquisition systems provided 15 days of continuous records including active source and ambient noise signals. A large vibroseis truck (T-Rex) was operated at 196 locations exciting a swept-frequency signal from 5 to 80 Hz over 20 seconds using three vibration modes. Sweeps were repeated up to four times during different modes of geothermal plant operation: normal operation, shutdown, high and oscillatory injection and production, and normal operation again. The cross-correlation method was utilized to remove the sweep signal from the geophone records. The first P arrivals were automatically picked from the cross-correlation functions using a combination of methods, and the travel times were used to invert for the 3D P-wave velocity structure.

Models with 50 m horizontal node spacing were obtained, with vertical node spacing of 10 to 50 m. The travel time data were fit to about 30 ms, close to our estimated picking uncertainty. Boundaries between high and low velocity zones agree with previous surveys of local faults and low velocity zones near the surface correspond to fumarole locations. A rapid increase in velocity at about 50 m depth

fits with borehole data on the depth of the Quaternary sediments. There is some evidence for changes in the P-wave velocity during the experiment with slower travel times at the beginning of the experiment.

Introduction

One of the major challenges with seismic tomography studies is the inherent uncertainty in using earthquakes as the source of seismic waves. We cannot control the spatial or temporal distribution of earthquakes so the resulting sampling of the earth is rarely ideal. By using controlled sources, we can choose the locations of our sources and recorders and thereby more accurately target our area of interest.

Controlled sources also eliminate the uncertainty of source location and time. The trade-off to these reductions in uncertainty is a reduction in source energy.

Controlled sources are also generally limited to the surface, which limits how deep the waves that reach our recorders have traveled. A vibroseis source offers many benefits as a controlled source. It is nondestructive, highly repeatable, and can be tailored to certain frequencies. Certain vibroseis sources also allow for different modes of vibration that produce stronger P or S waves.

PoroTomo Project

The Poroelastic Tomography by Adjoint Inverse Modeling of Data from Seismology, Geodesy, and Hydrology (PoroTomo) Project is an integrated, multidisciplinary assessment of methods for shallow geothermal reservoir characterization and monitoring. The natural laboratory of the Brady Hot Springs geothermal field was chosen as the field area for the PoroTomo Project in part due to the presence of multiple shallow subsidence signatures shown in satellite interferometric synthetic aperture radar (InSAR) (Ali et al., 2014) (Figure 1). The project's goal is to assess an integrated technology by characterizing a shallow

volume of the area where the subsidence is occurring using multiple geophysical methods.

Geologic Background

Several bands of geothermal fields stretch across the northwestern Great Basin in the US (Figure 2). The Humboldt geothermal belt is one such feature and includes several high-temperature geothermal systems with temperatures in excess of 160°C (Faulds et al., 2004). Volcanism in the region ceased between 3 to 10 Ma (Faulds et al., 2006) and many of the geothermal systems are considered to have amagmatic heat sources (Faulds et al., 2004). NNE-striking faults orthogonal to the direction of the regional extension are considered to be the primary control on the location and structure of the geothermal systems (e.g., Faulds et al., 2004, 2006, 2010a).

Most of the geothermal systems are hosted by steeply dipping normal fault zones where dilation facilitates deep circulation of thermal waters (Faulds et al., 2004, 2006). These normal fault zones appear to be more favorable for hosting geothermal systems than major range-front faults (Faulds et al., 2006). In particular, local features such as stepovers and intersections of fault zones are the common sites of geothermal systems (Faulds et al., 2004). Faulds et al. (2003) suggest that the small component of sinistral shear associated with many en echelon overlapping normal faults combined with the regional extension leads to locally greater fault and fracture density. Favorable stratigraphic units would also be integral for localizing geothermal reservoirs and facilitating fluid transmissivity (Faulds et al., 2003).

Brady geothermal field is located in the Hot Springs Mountains. The geology of the region consists of Mesozoic plutonic-metamorphic basement overlain by late Oligocene to late Miocene volcanic and sedimentary rocks (Faulds and Garside, 2003; Faulds et al., 2010a, 2010b, 2012). The Hot Springs Flat basin that lies to the west of the Hot Springs Mountains consists of late Miocene to Quaternary basin-fill sediments with the Quaternary sediments dominated by lacustrine deposits (Faulds and Garside, 2003; Faulds et al., 2010a, 2010b, 2012). The region is broken into multiple NNE-trending fault blocks by NNE-striking normal faults, with multiple dating methods indicating the major episode of extension occurred from 13 to 9 Ma (Faulds et al., 2006, 2010b).

Three major fault systems host the three major geothermal anomalies of the northern Hot Springs Mountains: Brady Hot Springs, Desert Peak, and Desert Queen (Benoit et al., 1982; Faulds et al., 2010b). Spaced approximately 5 km apart (Figure 3), their proximity suggests a shared heat source although their geologic relationship is uncertain (Benoit et al., 1982; Faulds et al., 2010b). Water chemistry from Brady and Desert Peak indicates the systems are independent (Benoit et al., 1982). The Brady fault zone forms the northwestern boundary of the Hot Springs Mountains and is the main structural control in the Brady geothermal field (Faulds et al., 2010a), which dips 60-80° to the NW (Jolie et al., 2015) with the main Brady fault accommodating 150 m of throw (Benoit et al., 1982; Faulds et al., 2003). Brady is the only geothermal system in the northern Hot Springs Mountains that is not a blind system (Benoit et al., 1982; Faulds et al., 2010b), and its surface expression

extends 4 km along the Brady fault as fumaroles, warm ground, sinter deposits, and mud pots (Figure 4) (Faulds et al., 2010a, 2010b; Jolie et al., 2015).

Brady Hot Springs geothermal field is a high enthalpy geothermal system (Faulds et al., 2010a) with an estimated reservoir temperature of 181°C (Shevenell and DeRocher, 2005). From the 1930s to the 1950s, it was the site of a resort and spa (Benoit et al., 1982) and in 1978 it became the site of the world's first geothermal food processing plant (Faulds et al., 2010b). A combined flash and binary geothermal power plant began operation in 1992 with an installed capacity of 26.1 MWe (Ettinger and Brugman, 1992; Shevenell et al., 2012). Production wells penetrate a small left step in one of the major splays in the Brady fault zone at a depth of 600-1500 m below surface level (Faulds et al., 2006; Jolie et al., 2015). Although permeability is necessary for a geothermal system, high transmissivity has led to problems with the production operations at Brady including short fluid residence times between injection and production wells and excessive drawdown in existing wells (Faulds et al., 2003).

Data & Methods

The PoroTomo Project deployed several arrays at the Bradys Geothermal Natural Laboratory in March 2016. In conjunction with that deployment, the production operation of the geothermal was varied to produce four different periods of injection and production activity. These four periods of different activity became the four stages of this experiment. The first stage was characterized by normal levels of production, the second stage was characterized by no production

with limited fluid extraction from or injection into the reservoir, the third stage was characterized by high and variable levels of production, and the fourth stage was characterized by a return to normal production activity.

The seismic array was deployed over a 1.6 km by 1.3 km area with a central array of 1.6 km by 0.5 km with approximately 60 m spacing and the exterior portions of the array having approximately 200 m spacing (Figure 5). Instrumentation included 240 5 Hz three-component nodal geophones, although data could only be recovered from 238 instruments. Additionally, 6 three-component Reftek instruments with 4.5 Hz geophones were deployed around the perimeter of the inner array, co-located with nodal geophones (Figure 5). Data from the Reftek instruments were regularly retrieved to provide a signal quality check during fieldwork operations. The acquisition systems provided 15 days of continuous records.

A large vibroseis truck, nicknamed T-Rex, generated the active source seismic signals for this experiment. It was operated at 196 locations, occupying each location up to four times over the course of 15 days, once for each stage (Figure 5). It excited a swept-frequency signal from 5 to 80 Hz over 20 seconds using three vibration modes: compressional, shear longitudinal, and shear transverse. Each mode of vibration was repeated at least three times for each site occupation. In total, there were 6,633 vibroseis events.

8700 m of 6.1 mm abrasion and rodent resistant fiber optic cable with acrylate-coated fibers rated to 85°C was deployed in backfilled trenches throughout the field area for the purpose of distributed acoustic sensing (DAS) (Figure 6). DAS

is a recently developed technology that has primarily been used for vertical seismic profiling (VSP) (Mateeva et al., 2014; Mestayer et al., 2011) in oil and gas reservoirs but has also been used in small-scale surface deployments (Daley et al., 2013; Zeng et al., 2016; Lancelle, 2016; Castongia et al., 2017). Sampling was recorded through a SILIXA interrogator system with a spatial averaging window of 10 m recorded at approximately every meter along the cable. 370 m of 1/8" FIMT cable with carbon-polyimide-coated fibers rated to 150°C was also deployed down an observation well (Figure 6) to provide sampling to greater depths, but due to deployment delays it was only installed in time to record Stages 3 and 4. Coupling of the borehole cable to the formation was poor and limited to direct contact where the cable rests against the borehole walls and by air or water where it was free hanging.

Vibroseis Sweep Removal

While swept frequency sources have the advantage of repeatability, the non-impulsive nature of a swept-frequency source makes it difficult to determine the first arrival of seismic waves. In order to see the equivalent of a first arrival, one must first remove the swept-frequency signal from the waveforms. To this end, several different methods have been developed (Brittle et al., 2001; Ikuta et al., 2002; Saiga et al., 2006; Li et al., 2013). The two most common methods are cross-correlation and deconvolution (Brittle, 2001). Both methods were applied to real data and then compared to determine the best method for this dataset.

Cross-correlation

The cross-correlation of the source sweep with the recorded signal produces a waveform with peaks at the arrival times for the seismic waves. The relationship of the source sweep and recorded data can be expressed as

$$x(t) = r(t) * s(t), \quad (1.1)$$

where $x(t)$ is the geophone record, $s(t)$ is the source sweep, $r(t)$ is the Green's function and instrument response, and $*$ represents the convolution.

Cross-correlating the observed data, expressed as the convolved source sweep and ground response, with the source sweep produces

$$cc(t) = r(t) * s(t) \otimes s(t) \quad (1.2)$$

where $cc(t)$ is the result of the cross-correlation and \otimes represents the cross-correlation operator. The autocorrelation of a linear vibroseis sweep is defined as a Klauder wavelet (Sheriff, 2002). Equation (1.2) can be simplified to

$$cc(t) = r(t) * k(t) \quad (1.3)$$

where $k(t)$ is the Klauder wavelet. The Klauder wavelet is a zero-phase wavelet whose shape depends on the sweep design.

When taking the effect of noise, $n(t)$, into account, (1.1) becomes

$$x(t) = r(t) * s(t) + n(t) \quad (1.4)$$

and (1.3) becomes

$$cc(t) = r(t) * k(t) + n(t) \otimes s(t). \quad (1.5)$$

The Klauder wavelet is still present, but the noise is cross-correlated with the sweep. Since cross-correlation measures similarity, frequencies in the noise outside

of the sweep tend to be filtered out. Regardless, applying a band-pass filter before cross-correlating improves signal resolution (Figure 7).

Deconvolution

Deconvolution is a frequency-domain inversion technique that has become common for vibroseis sweep removal. As an inversion technique, given perfect data it is possible to return a perfect result [Brittle, 2001], however this is rarely the case.

Since convolution in the time-domain is equivalent to multiplication in the frequency domain, (1.1) can be expressed as

$$X(\omega) = S(\omega)R(\omega), \quad (1.6)$$

where ω is the angular frequency and X, S, and R are Fourier transforms of x, s, and r. By using element-by-element division, indicated by the symbol \oslash , (1.6) becomes

$$R(\omega) = X(\omega) \oslash S(\omega). \quad (1.7)$$

Alternatively, (1.7) can be written in terms of frequency-domain sweep deconvolution (FDSD)

$$FDSD(\omega) = \frac{X(\omega)}{S(\omega)} = \frac{S(\omega)R(\omega)}{S(\omega)} \quad (1.9)$$

When noise is taken into consideration, (1.6) can be written as

$$X(\omega) = R(\omega)S(\omega) + N(\omega). \quad (1.10)$$

When the sweep is removed in the frequency domain, the noise is also divided by the sweep

$$X_{FDSD}(\omega) = \frac{R(\omega)S(\omega)}{S(\omega)} + \frac{N(\omega)}{S(\omega)} \quad (1.11)$$

This has the effect of amplifying the noise for frequencies not included in the source sweep or those with very low amplitude. This noise amplification can be managed

by applying a band-pass filter to the recorded waveform before deconvolution (Figure 8).

Comparison

The results of cross-correlation and deconvolution are generally quite similar (Figure 9). The clearest difference is that there is more high frequency noise in the deconvolution results. At greater distances from the source, low frequency noise also becomes apparent in the deconvolution results (Figure 10). Additional filtering might reduce the noise levels in the deconvolution, but since the cross-correlation results have less noise to begin with, using the cross-correlation method to remove the vibroseis signal from the waveforms was favored.

The next step was to stack the cross-correlation waveforms to further improve the signal to noise ratio. Stacks involved all instances of a sweep mode at a vibe point for each stage of the experiment. Stacking occurred after cross-correlation, as the source waveform was unique for each sweep. The sweep signal failed to record for a few sweeps and in those cases the pilot sweep was used. The pilot sweep was the waveform the vibroseis truck was programmed to produce. Although it was missing the ground coupling effects that are included when using the actual sweep signal produced, the cross-correlation results are almost identical to using the recorded sweep waveform (Figure 11).

Automatic Arrival Time Picker

In order to process the large volume of waveforms and to maximize the number of picks, it was necessary to use an automatic phase arrival picker. There is

no standard autopicking method used for cross-correlated vibroseis waveforms, so we tested several autopickers using a data subset of three spatially separated vib points during Stage 2. Stage 2 was chosen as it had the lowest level of background noise. The autopickers were then narrowed down to the three with the highest number of picks within a window where P-wave arrivals were most likely to be present.

These autopickers were: an Akaike information criterion (AIC) algorithm (Sleeman and Van Eck, 1999; Akram and Eaton, 2016), a short- and long-time average ratio (STA/LTA) algorithm (Trnkoczy, 2009; Akram and Eaton, 2016), and a deep neural network (DNN) seismic autopicker (Bin Guo, personal communication, 2017). The AIC and STA/LTA algorithms were sourced from Akram and Eaton (2016) and were not modified. The DNN autopicker was trained using manual picks of the first significant peak in the P-wave arrival train. The peaks of cross-correlation waveforms are where arrivals are most likely to occur as opposed to standard seismograms where an arrival is at the onset of arrival waveforms. Thus, the DNN autopicker has the advantage of not being biased to pick before the true arrival time like both the AIC and STA/LTA methods, which pick the onset of arrival waveforms. No corrections were made to the pickers that picked the onsets rather than the peaks because the potential increase in accuracy would be less than the inherent uncertainty of the autopickers.

To compare how well the autopickers identified the P-wave arrivals, they were run on 45 vib points from Stage 2 selected for having clear arrivals and a roughly even distribution over the array. The autopicks were then filtered based on

whether the times fell within a window of “acceptability” based on the distance from the source to the instrument and the apparent velocity of the P-wave. The window was expanded with distance to accommodate variation in travel times and so that the window didn’t have to be tailored to the slope of travel times for each vibe point. 59.94% of AIC picks (Figure 12), 53.21% of STA/LTA picks (Figure 13), and 46.33% of DNN picks (Figure 14) fell within the bounds of reasonable travel times. After retraining the DNN to pick the onset of arrivals, its success rate rose to 58.69%.

Due to its higher rate of success and greater consistency, we chose to use the AIC autopicker. To improve the quality of the picks, we ran a tomographic inversion using the picks that fell within the likely travel time range. From that model we generated predicted travel times. A new set of “acceptability” windows set 0.1 s before and 0.2 s after the predicted travel time for each receiver-source pair. These new bounds were able to account for variations in travel time, with slow arrivals being more likely than early arrivals, while reducing the size of the window on average. Subsequent runs of the autopicker picked the best time within that window.

After applying the AIC autopicker to more data, it became clear that it struggled to correctly pick the P-wave arrival for waveforms from stations within 150 m of the source due to a bias in the algorithm. It was often picking the airwave arrival instead of the P-wave arrival due to the greater energy of the airwave at those distances. To obtain these near distance arrivals, we decided to use a different autopicker when the recorder was within 150 m of the source. We opted to use the STA/LTA autopicker rather than the DNN autopicker. Although the STA/LTA was

less successful on average at picking arrivals, it was well suited for the near distance waveforms with their high signal to noise ratios. The final number of picks was: 44,268 for Stage 1; 38,719 for Stage 2; 41,520 for Stage 3; and 42,518 for Stage 4.

To weight the travel time picks from the nodal data for the tomographic inversion, signal to noise ratios (SNR) were measured for each pick. These SNR values were calculated by dividing the root means square (RMS) of a windows 0.2 s after the pick time by the RMS of a 0.2 s window before the pick. The noise window was chosen to be directly before the pick rather than at a fixed time with no signal because it was desirable to penalize picks of the airwave arrival rather than the P-wave arrival. Due to the strength of the airwave arrival in some of our waveforms, a standard SNR noise window would have a good SNR value for an airwave arrival, whereas using a noise window directly before the airwave pick would include the energy from the P-wave arrival and reduce the SNR.

The same AIC autopicker was applied to the vertical and horizontal DAS (DASV and DASH) records using channels every 5 m to balance the amount of overlap in signals due to the 10 m sampling window while maximizing the number of receiver locations at depth. Channels from 166 m to 346 m along the length of the DASV cable were used because this was the length of the cable that showed the best coupling with the well and therefore the clearest signals. The SNR of the vibe source was only high enough to pick arrivals for the 17 nearest source locations. For Stage 3 there were 305 picks, and for Stage 4 there were 323. Channels every 10 m were used from the horizontal DAS array. For Stage 4, 45,989 arrivals were picked. SNR

ratios for each point were measured using a set noise window since the airwave did not complicate the P-wave arrival in the DAS data..

Tomographic Inversion

To obtain a 3D V_p model, we used the simul2000 tomography code (Thurber and Eberhart-Phillips, 1999). Simul2000 ignores the curvature of the Earth's surface, so source and receiver locations were transformed into a Cartesian coordinate system centered on the southwest corner of the denser portion of the nodal seismometer array at 39.8010°N and 119.0108°W , with the X axis oriented at about 36° azimuth. The inversion grid for the final model is 2.0 km long in the X direction and 1.3 km wide in the Y direction, with horizontal node spacing of 50 m except for the outside edges where the spacing is 100 m. Nodes in the Z direction are located at 0.00, 0.02, 0.04, 0.06, 0.10, 0.15, 0.20, 0.25, 0.35, 0.45, and -0.65 km with 0 km corresponding to 1250 m above the WGS84 ellipsoid, which is approximately equal to the lowest point in the array. A list of travel time picks is given as an input into the program, so it was simple to include the travel times picked from all three arrays in one input list. In this way simul2000 doesn't differentiate between the different sources of data.

Tomography algorithms are regularized, non-linear inverse problems that use damping and/or smoothing parameters that govern the trade-off between data misfit and model perturbations and roughness. The simul2000 code provides complete information on model resolution and uncertainty. We chose to select the damping value that yielded acceptably high resolution and acceptably low

uncertainty values with a reasonable final misfit to the data. Comparing the model results, final misfit, resolution, and uncertainties from damping values of 0.04, 0.1, and 1, a damping value of 0.1 had the best trade-off with low uncertainties and reasonable detail of features in the model results without excessive oscillations in velocity. In contrast, the model with 0.04 damping had unrealistically large, oscillatory velocity variations with unacceptably high model uncertainties, and the model with damping of 1 did not fit the data as well, had rather small velocity variations, and unacceptably poor model resolution.

Results & Discussion

Figure 15 shows depth slices and Figure 16 shows cross-sections of the V_p model for Stage 4 for an inversion that used P-wave arrival picks from the nodal seismometers, DASH, and DASV. In the shallower depth slices, low velocity zones dominate the model. These velocities are consistent with the expected values of the alluvial deposits found at the surface. Based on well lithologies, these alluvial deposits extend to depths of approximately 50 m (Figure 17). This depth is consistent with a transition from slower to faster velocities in the velocity model (Figure 16) and is too shallow to be the water table, which is around 100 m depth. Since the water table is located in a fracture-dominated environment, its location is not apparent in the velocity model. The faster velocities at depth fall within the reported seismic velocities for tuff (Wohletz and Heiken, 1992) and sedimentary deposits (Bourbié and Coussy, 1987). Abrupt lateral changes in velocity are

attributed to the presence of faults juxtaposing rocks with different seismic velocities.

Several features are most apparent in the 60 m depth slice. A low velocity zone can be seen transecting the field in a north-south direction near the southwestern corner of the natural laboratory. A second low velocity zone extends from the south edge of the array up to the northern corner with a slightly more NE-SW orientation in the northern half. Between the two low velocity zones is a high velocity zone. A larger high velocity zone parallels the longer low velocity zone. In deeper depth slices, we start to have reduced resolution but the contrast between the larger low and high velocity zones persists.

General trends in the structure match the results from other models. Figure 18 shows the results of V_p and V_s models using shot interferometry noise tomography of PoroTomo data (Eric Matzel, personal communication, March 2017). High and low velocity zones follow the same NE-SW trend across the field area with a bend to a more N-S orientation in the southwestern portion of the field area. There is less detail in the ambient noise models and higher contrast in the active source model. The active source model depth slice at 60 m depth is at about the same depth as the ambient noise model depth slice $Z = 0.05$ km; they share the same features, but they appear compressed in the NW-SE direction in the shot interferometry noise model. The high velocity zone from $X = -200$ to 0 m and $Y = -100$ to 300 m is an example of differing locations for the same feature.

These low and high velocity zones are presumed to be bounded by splays in the Brady Fault Zone. In the surface level depth slice, there is a high velocity zone in

the southern corner of the array situated between two faults from (800, 400) to (900,0). In deeper slices of the model, the high velocity zone expands and is no longer bounded between the fault splays. However, it continues to be bounded by the longer of the fault splays, and by 60 m depth it is bounded by the next fault splay to the west. This western boundary persists through 100 m depth as the low velocity extends farther north. Continuing deeper into the model, the fault traces do not align with the edges of the high velocity zone and at 200 m depth the correlation is lost.

In general, the 60 m depth slice has the strongest correlation between the fault traces and the high and low velocity zones. Most of the fault traces correspond to boundaries between high and low velocity zones and keep these relationships in the shallower and/or deeper slices of the model. The biggest exception is the fault splay that strikes SW along $X = 150$ m from $Y = 700$ to 1700 m. This fault consistently lies in the middle of a high velocity zone through the various layers of the model. This suggests it is a minor splay compared to the others, or that its displacement is offsetting rock units of similar seismic velocity. The other fault splay that doesn't correspond to a contrast in seismic velocity strikes SW at from $X = -200$ to -100 m and $Y = 200$ to 1600 m. This splay and the splay directly west of it do mark the boundary of a zone that is relatively faster than the surrounding model at shallow depths but is relatively slower at greater depths with the transition happening at about 60 m depth, as seen in the $Y = 1400$ m depth profile (Figure 15).

The locations of the geothermal surface features, fumaroles and warm ground, roughly follow the step-overs in the fault splays in the southwestern part of

the field area (Figure 4). They extend from about (150, 400) to (400, 0), dispersed through the area between the two splays that branch out from (150, 400). This does not correspond to the slowest parts of the surface level part of the model, but they are adjacent to the slowest parts of the model in the slice that is approximately 20 m below the surface although they are underlain by a high velocity zone 40 m below the surface. This suggests their location is controlled by a fault that offsets layers in the subsurface that channels the steam that feeds the fumaroles, but that the conduits near the surface are controlled more by the permeability of the surface sediments.

The subsidence seen in the interferograms is roughly where a mostly low velocity zone in the center of the field area is in the 60 m depth slice. It is bounded by faults to the southeast that extend from (200, 1100) to (400, 100) and to the northwest from (100, 1100) to (100, 100). If the subsidence was due to contraction of the rock as the shallow part of the reservoir cooled, as proposed by Ali et al. (2014), then the higher velocity areas on the northeast portion of the zone could be due to the cooling temperatures and the lower velocity portion might be where the shallow reservoir was still warm and connected to the conduits feeding the fumaroles. The cross-section for $Y = 600$ m shows the spatial relationship between the high and low velocity zones with depth.

Queen et al. (2016) carried out a seismic reflection and vertical seismic profile survey of Brady Hot Springs focusing on the part of the geothermal field around the production wells. Figure 17 shows their results for a profile just south of our field area. Although their profiles are deeper, the depths at which we see

changes in seismic velocity tend to agree (Figure 16). At about 50 m depth our model shows a rapid increase in seismic velocity that corresponds to the depth of the base of the Quaternary units from the wellbore lithology. Velocities of around 2.5-3 km/s occur at depths of about 150 m.

Temporal change

Evidence for change in seismic velocity over the course of the experiment can be seen by looking at the arrival time picks for each stage at each vibe point. Figure 19 compares the arrival times for the nodal stations for each stage of the experiment for representative vibe points. Although most of them have later arrivals during Stage 1, that is not always true. VP 121 has no discernable difference in arrival times between stages except that the outliers for Stage 1 tend to be slower. VP 133 has earlier Stage 1 arrivals than the other stages at near distances but slower Stage 1 arrivals at farther distances, with the switch happening at around 450 m distance. Although some vibe points seem to have slight differences in arrival times among Stages 2, 3, and 4, it is not distinct nor consistent enough to be clear evidence for a change in seismic velocity between those stages. Overall, the comparison of travel times for different stages is inconclusive and further work would be needed using other methods of comparison to determine if there is any change in the seismic velocity and, if so, where and of what magnitude.

Conclusion

We have presented P-wave velocity tomography results for the Brady Hot Springs geothermal field using active source data from a combined array of DAS and

nodal seismometers. Cross-correlation proved to be better than deconvolution for removing the vibroseis sweep signal from the recorded waveforms for this dataset. Autopickers were successful at picking the P-wave arrival for both types of data acquisition although the downhole DAS had a very limited range of distance to the vial location for which the arrivals were discernable. The P-wave velocity model showed clear delineations between high and low velocity zones that generally agree with past fault surveys (Jolie, 2014; Jolie et al., 2015). Low velocity zones near the surface correspond to fumarole locations and there is a rapid increase in velocity at depths that correspond with the bottom of the Quaternary sediments. There is inconclusive evidence for changes in the P-wave velocity during the experiment with arrival times during Stage 1 being slightly slower compared to the other stages, but there is no clear evidence for temporal change in seismic velocity between the later stages.

References

- Akram, J., and D. W. Eaton (2016), A review and appraisal of arrival-time picking methods for downhole microseismic data, *Geophysics*, **81**(2), KS67-KS87.
- Ali, S. T., N. C. Davatzes, P. S. Drakos, K. L. Feigl, W. Foxall, C. W. Kreemer, R. J. Mellors, H. F. Wang, and E. Zemach (2014), InSAR measurements and numerical models of deformation at Brady Hot Springs geothermal field (Nevada), 1997-2013, *Proceedings: 39th Workshop on Geothermal Reservoir Engineering, Stanford University, Stanford, California, February 24-26, 2014* SGP-TR-202, 14 p.
- Benoit, W., J. Hiner, and R. Forest (1982), Discovery and geology of the Desert Peak geothermal field: a case history, *Nevada Bureau of Mines and Geology Bulletin*, **97**, 82 p.
- Bourbié, T., and O. Coussy,(1987), *Acoustics of Porous Media*. Éd. Technip, Paris.
- Brittle, K. F. (2001), *Vibroseis deconvolution: frequency-domain methods* (Master's Thesis), University of Calgary, Alberta,174 p.
- Brittle, K. F., L. R. Lines, and A. K. Dey (2001), Vibroseis deconvolution: a comparison of cross-correlation and frequency-domain sweep deconvolution, *Geophysical Prospecting*, **49**(6), 675–686.
- Castongia, E., H. F.Wang, N. Lord, D. Fratta, M. Mondanos, and A. Chalari (2017), An Experimental Investigation of Distributed Acoustic Sensing (DAS) on Lake Ice. *Journal of Environmental and Engineering Geophysics*, **22**(2), 167-176.
- Daley, T. et al. (2013), Field testing of fiber-optic distributed acoustic sensing (DAS) for subsurface seismic monitoring, *The Leading Edge*, **32**(6), 699–706, doi:10.1190/tle32060699.1.
- Ettinger, T., and J. Brugman (1992), Brady Hot Springs Geothermal Power Plant, *Geothermal Resources Council Bulletin*, **12**(8), 259–260.
- Faulds, J. E., A. R. Ramelli, L. J. Garside, M. F. Coolbaugh, and H. L. Green (2012), Preliminary Geologic Map of the Desert Peak Quadrangle, Churchill County, Nevada, *Nevada Bureau of Mines and Geology*, Open-File Report 12-5.

- Faulds, J. E., and L. J. Garside (2003), Preliminary Geologic Map of the Desert Peak - Brady Geothermal Fields, Churchill County, Nevada, *Nevada Bureau of Mines and Geology*, Open-File Report 03-27.
- Faulds, J. E., L. J. Garside, and G. L. Oppliger (2003), Structural analysis of the Desert Peak-Brady geothermal field, Northwestern Nevada: implications for understanding linkages between Northeast-trending structures and geothermal reservoirs in the Humboldt structural zone, *Geothermal Resources Council Transactions*, **27**, 859–864.
- Faulds, J. E., M. Coolbaugh, G. Blewitt, and C. D. Henry (2004), Why is Nevada in Hot Water? Structural Controls and Tectonic Model of Geothermal Systems in the Northwestern Great Basin, *Geothermal Resources Council Transactions*, **28**, 649–654.
- Faulds, J. E., M. F. Coolbaugh, G. S. Vice, and M. L. Edwards (2006), Characterizing Structural Controls of Geothermal Fields in the Northwestern Great Basin: A Progress Report, *Geothermal Resources Council Transactions*, **30**, 69–76.
- Faulds, J., I. Moeck, P. Drakos, and E. Zemach (2010a), Structural assessment and 3D geological modeling of the Brady's geothermal area, Churchill county (Nevada, USA): A preliminary report, *Proceedings: 35th Workshop on Geothermal Reservoir Engineering, Stanford University, Stanford, California, February 1-3, 2010* SGP-TR-188, 298-302.
- Faulds, J. E., M. F. Coolbaugh, D. Benoit, G. L. Oppliger, M. Perkins, I. Moeck, and P. Drakos (2010b), Structural controls of Geothermal Activity in the Northern Hot Springs Mountains, Western Nevada: the Tale of Three Geothermal Systems (Brady's, Desert Peak, and Desert Queen), *Geothermal Resources Council Transactions*, **34**, 675–683.
- Ikuta, R., K. Yamaoka, K. Miyakawa, T. Kunitomo, and M. Kumazawa (2002), Continuous monitoring of propagation velocity of seismic wave using ACROSS, *Geophysical research letters*, **29**(13). 5 p.

- Jolie, E. (2014), Detection and characterization of permeable fault zones by surface methods in the Basin-and-Range Province, USA (Doctoral Thesis), Technische Universität, Berlin, 132 p.
- Jolie, E., I. Moeck, and J. E. Faulds (2015), Quantitative structural–geological exploration of fault-controlled geothermal systems—A case study from the Basin-and-Range Province, Nevada (USA), *Geothermics*, **54**, 54–67.
- Lancelle, C. (2016), Distributed Acoustic Sensing for Imaging Near-Surface Geology and Monitoring Traffic at Garner Valley, California (Doctoral Thesis), University of Wisconsin, Madison, 108 p.
- Li, Z., Q. You, S. Ni, T. Hao, H. Wang, and C. Zhuang (2013), Waveform retrieval and phase identification for seismic data from the CASS experiment, *Pure and Applied Geophysics*, **170**(5), 815–830.
- Mateeva, A. et al. (2014), Distributed acoustic sensing for reservoir monitoring with vertical seismic profiling, *Geophysical Prospecting*, **62**(4), 679–692, doi:10.1111/1365-2478.12116.
- Mestayer, J. et al. (2011), Field trials of distributed acoustic sensing for geophysical monitoring, in *SEG Technical Program Expanded Abstracts 2011*, pp. 4253–4257, Society of Exploration Geophysicists, Tulsa, Oklahoma.
- Queen, J. H., T. M. Daley, E. L. Majer, K. T. Nihei, D. L. Siler, and J. E. Faulds (2016), Surface Reflection Seismic and Vertical Seismic Profile at Brady’s Hot Springs, NV, USA, *Proceedings: 41st Workshop on Geothermal Reservoir Engineering, Stanford University, Stanford, California, February 22-24, 2016* SGP-TR-209, 15 p.
- Saiga, A., K. Yamaoka, T. Kunitomo, and T. Watanabe (2006), Continuous observation of seismic wave velocity and apparent velocity using a precise seismic array and ACROSS seismic source, *Earth, planets and space*, **58**(8), 993–1005.
- Sheriff, R. E. (2002), *Encyclopedic Dictionary of Applied Geophysics*, 4th ed., Society of Exploration Geophysicists, Tulsa, Oklahoma.

- Shevenell, L., and T. DeRocher (2005), Evaluation of Chemical Geothermometers for Calculating Reservoir Temperatures at Nevada Geothermal Power Plants, *Geothermal Resources Council Transactions*, **29**, 303–308.
- Shevenell, L., J. G. Price, and R. H. Hess (2012), Data tables and graphs of geothermal power production in Nevada, 1985-2011, *Nevada Bureau of Mines and Geology*, Open-File Report 12-03.
- Sleeman, R., and T. van Eck (1999), Robust automatic P-phase picking: an on-line implementation in the analysis of broadband seismogram recordings, *Physics of the Earth and Planetary Interiors*, **113**(1), 265–275, doi:10.1016/S0031-9201(99)00007-2.
- Thurber, C., and D. Eberhart-Phillips (1999), Local earthquake tomography with flexible gridding, *Computers & Geosciences*, **25**, 809–818.
- Trnkoczy, A. (2009), Understanding and parameter setting of STA/LTA trigger algorithm, in *New Manual of Seismological Observatory Practice (NMSOP)*, pp. 965–984, Deutsches GeoForschungsZentrum GFZ, Potsdam.
- Wohletz, Kenneth, and Grant Heiken (1992), *Volcanology and Geothermal Energy*, University of California Press, Berkeley, California.
<http://ark.cdlib.org/ark:/13030/ft6v19p151/>
- Zeng, X., C. Lancelle, C. Thurber, D. Fratta, H. Wang, N. Lord, A. Chalari, and A. Clarke (2017), Properties of Noise Cross-Correlation Functions Obtained from a Distributed Acoustic Sensing Array at Garner Valley, California, *Bulletin of the Seismological Society of America*, **107**(2), doi:10.1785/0120160168.

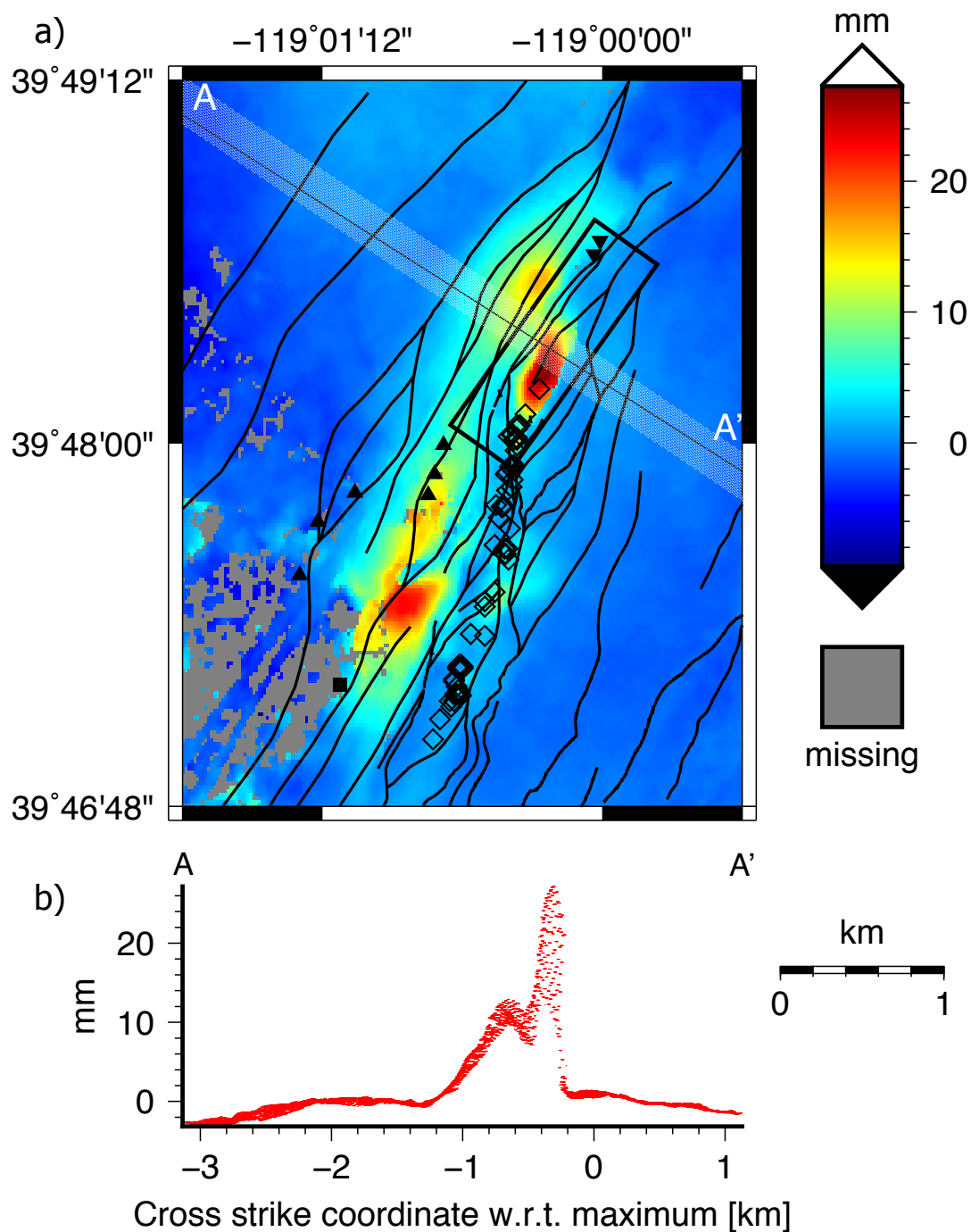


Figure 1. a) Profile plot of unwrapped range change from a TerraSAR-X track 53 pair spanning from November 24, 2011 – October 27, 2012. A positive change in range means an increased distance from the satellite and corresponds to subsidence. Triangles with point up for production wells, point down for injection wells, and black squares for observation wells. Hallow diamonds denote fumarole locations and black lines for faults traces. Large rectangle outlines the densest part of the seismometer array (Figure 5). b) Plot of the phase values for points within the shaded region along the A-A' profile. (Elena Reinisch, personal communication, July 21, 2017)

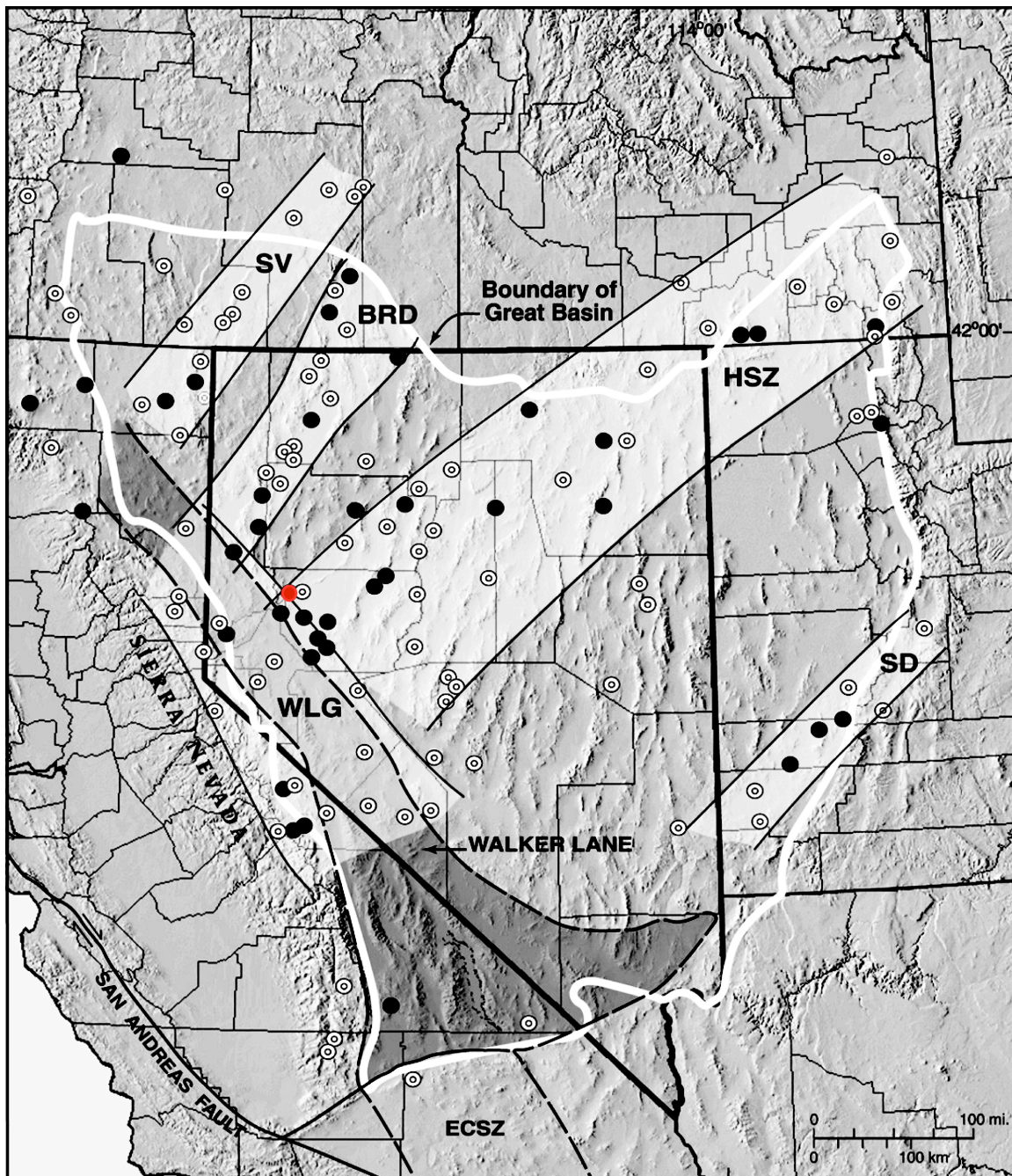


Figure 2. Map of geothermal fields in the Great Basin from Faulds et al. (2004). Geothermal field belts are the Sevier Desert (SD), Humboldt structural zone (HSZ), Black Rock Desert (BRD), Surprise Valley (SV), and Walker Lane (WLG). Circles are geothermal systems; white for maximum temperatures below 160°C and black for maximum temperature above 160°C. Red circle marks Brady Hot Springs geothermal field. ECSZ, eastern California shear zone.

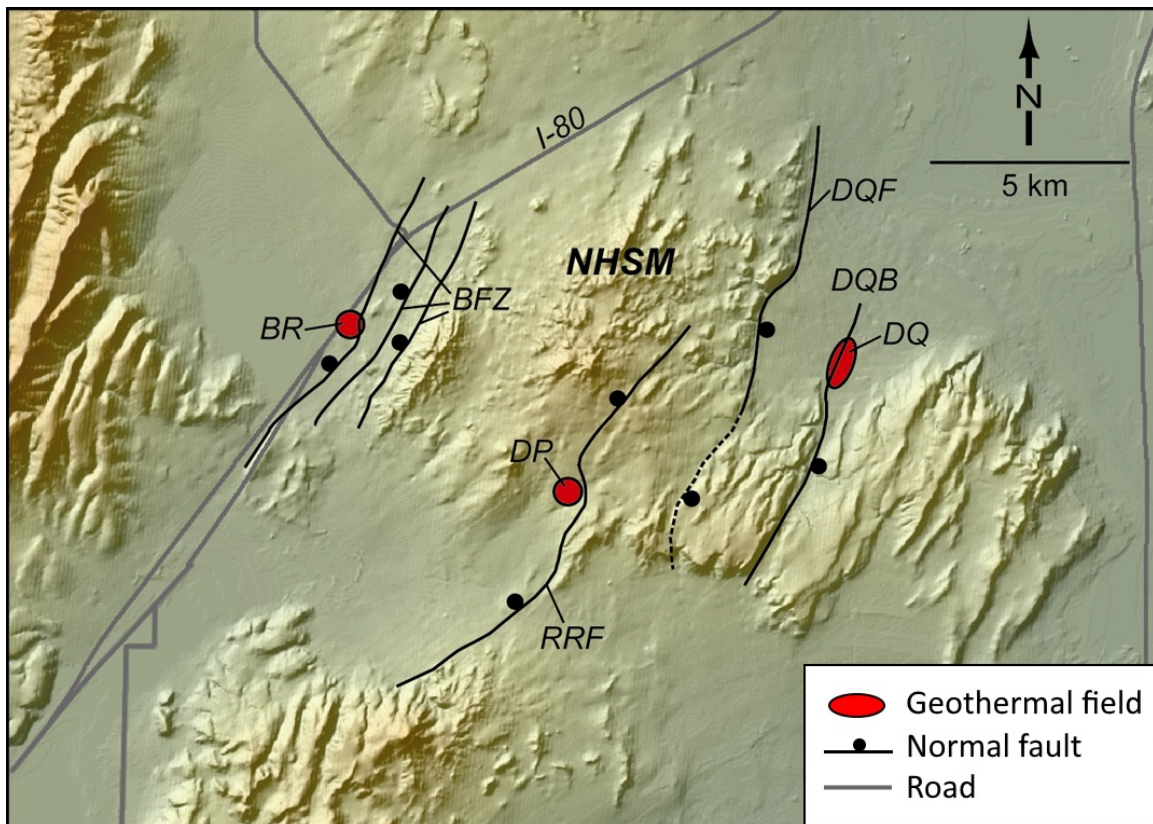


Figure 3. Digital elevation map of the northern Hot Springs Mountains (NHSM) from Faults et al. (2010b). The three major geothermal fields in the area are Brady Hot Springs (BR), Desert Peak (DP), and Desert Queen (DQ) and the areas with production wells are indicated by the red circles. Major faults are shown with the ball on the down-thrown block: Brady's fault zone (BFZ), Rhyolite Ridge fault zone (RRF), and Desert Queen fault zone (DQF). DQB, Desert Queen Basin.

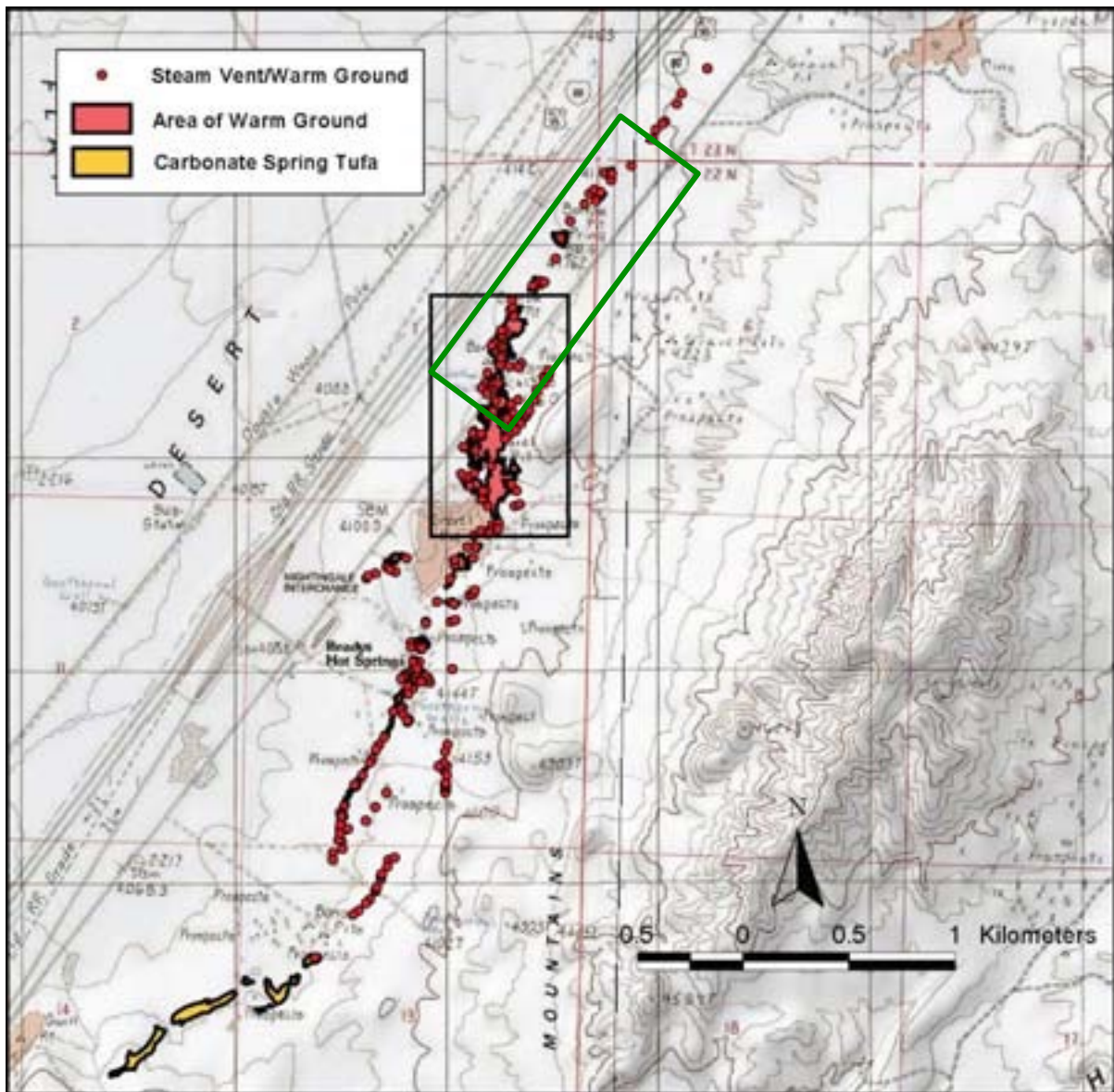


Figure 4. Map of geothermal surface features at Brady Hot Springs geothermal field from Faulds et al. (2010a). The green box corresponds to the densest part of the nodal seismometer array (Figure 5).

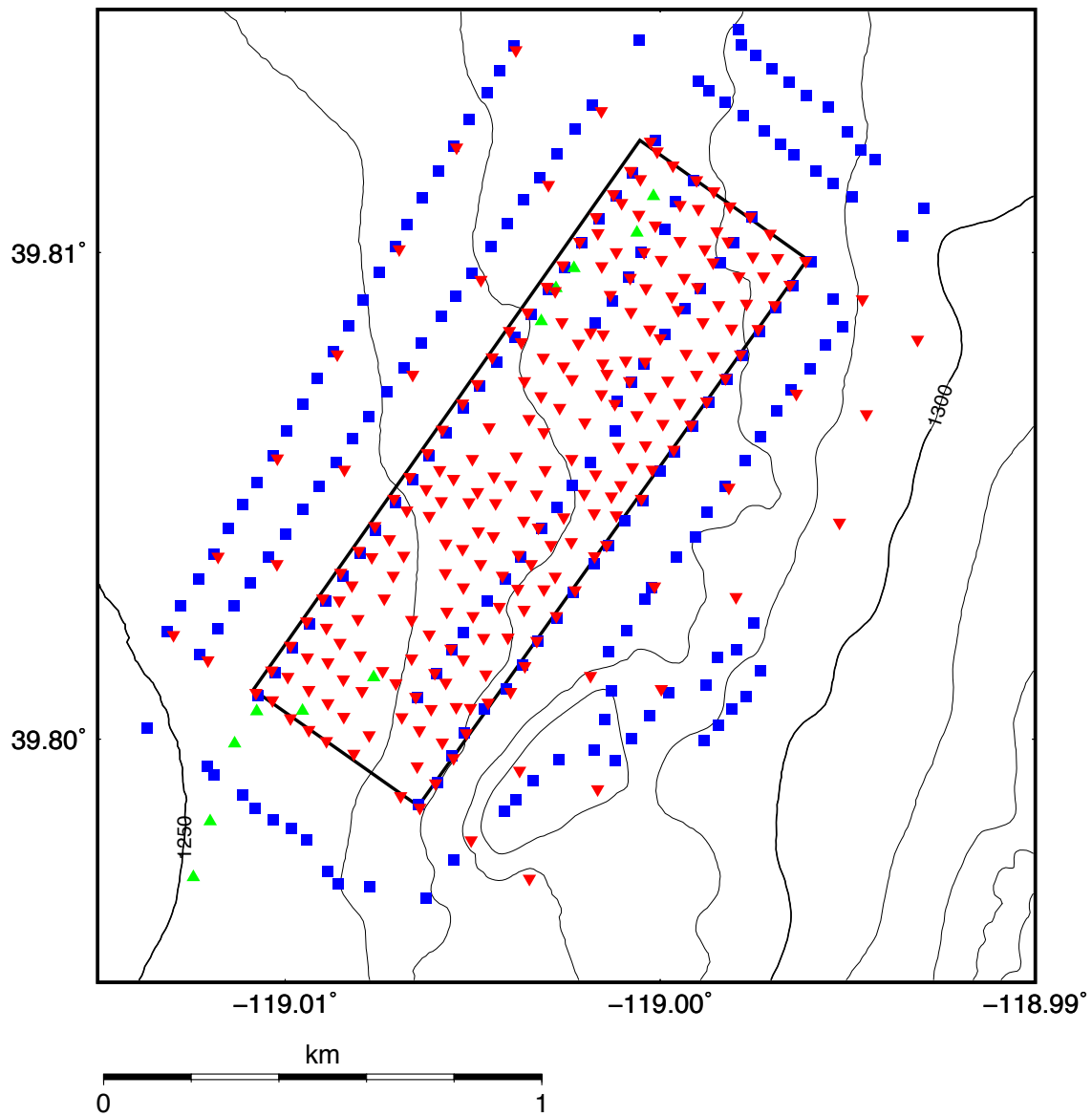


Figure 5. Map of seismometer array with 10 m elevation contour intervals. Red triangles are nodal seismometer locations. Blue squares are vibroseis locations. Green triangles are well locations.

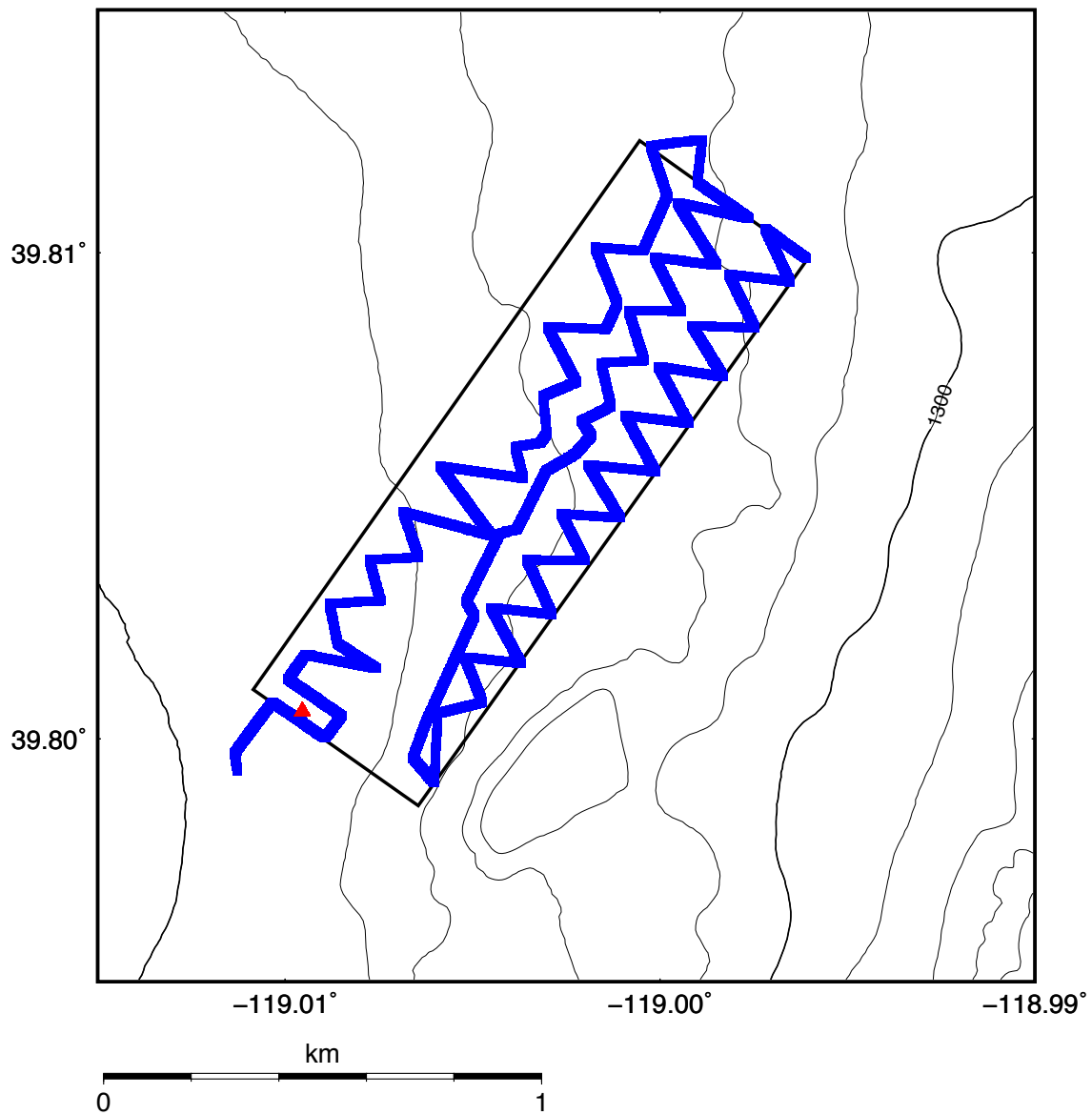


Figure 6. Map of DAS array with 10 m elevation contour intervals. The blue line is the surface array and the red triangle is the well with the vertical array. The black box is the outline of the densest part of the nodal seismometer array (Figure 5).

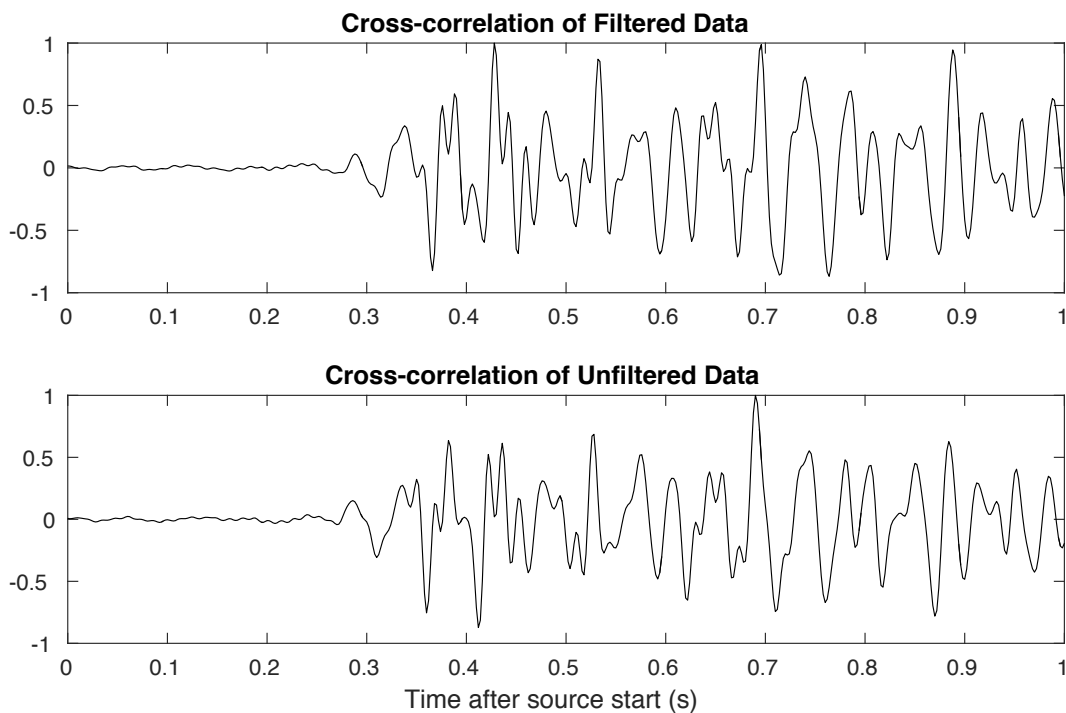


Figure 7. Results for a waveform with and without applying a bandpass filter to the recorded waveform before cross-correlation.

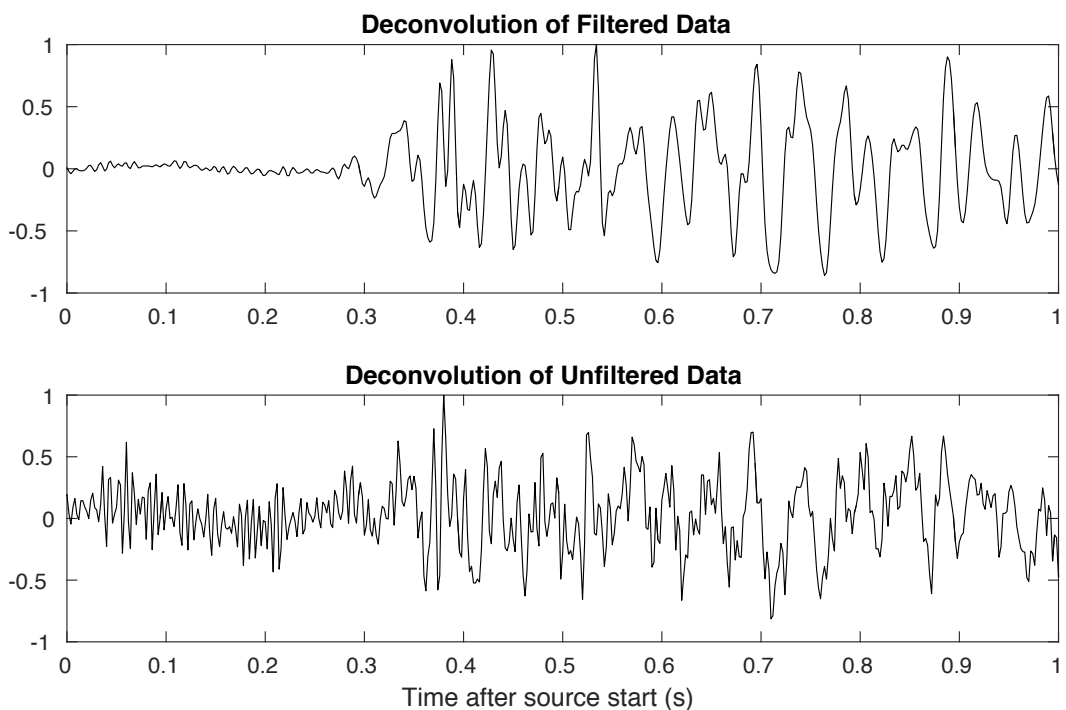


Figure 8. Results for a waveform with and without applying a bandpass filter to the recorded waveform before deconvolution.

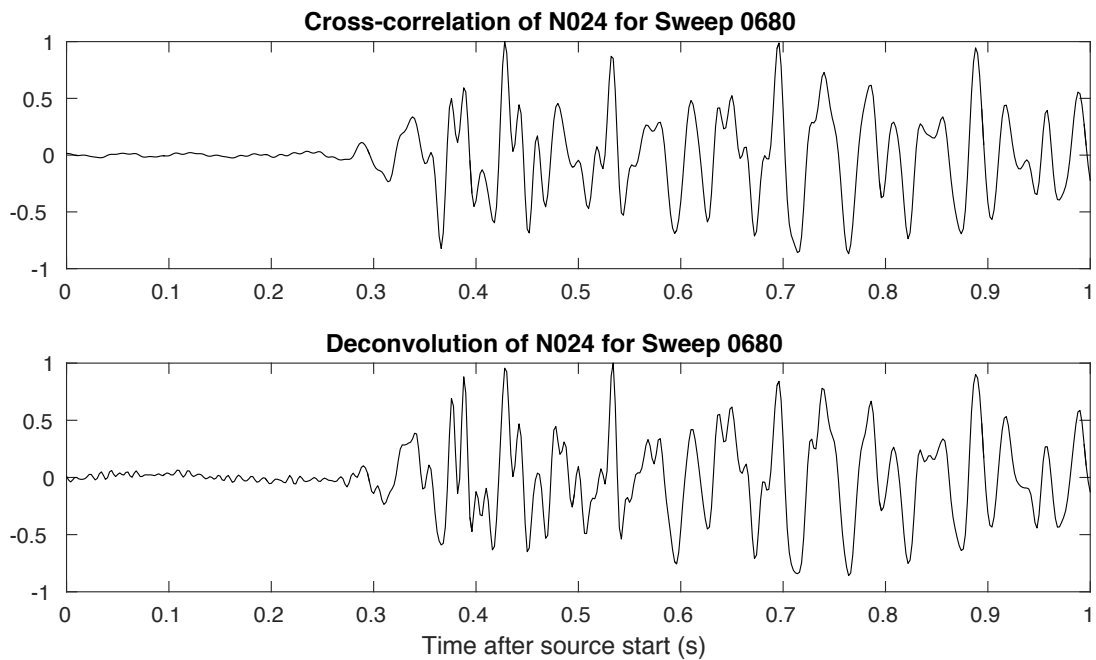


Figure 9. Results for cross-correlation and deconvolution using the same source and receiver waveforms show comparable waveforms with more high frequency noise in the deconvolution results. The distance between source and receiver is 440.3 m.

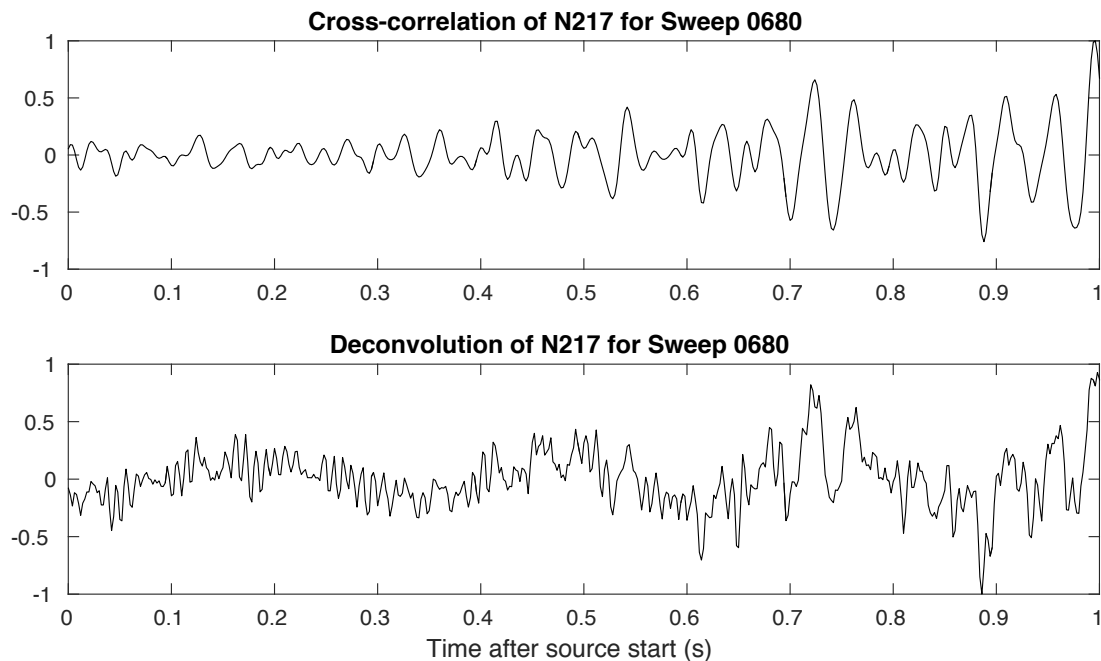


Figure 10. Results for cross-correlation and deconvolution using the same source and receiver waveforms show more high frequency and low frequency noise in the deconvolution results. The distance between source and receiver is 811.0 m.

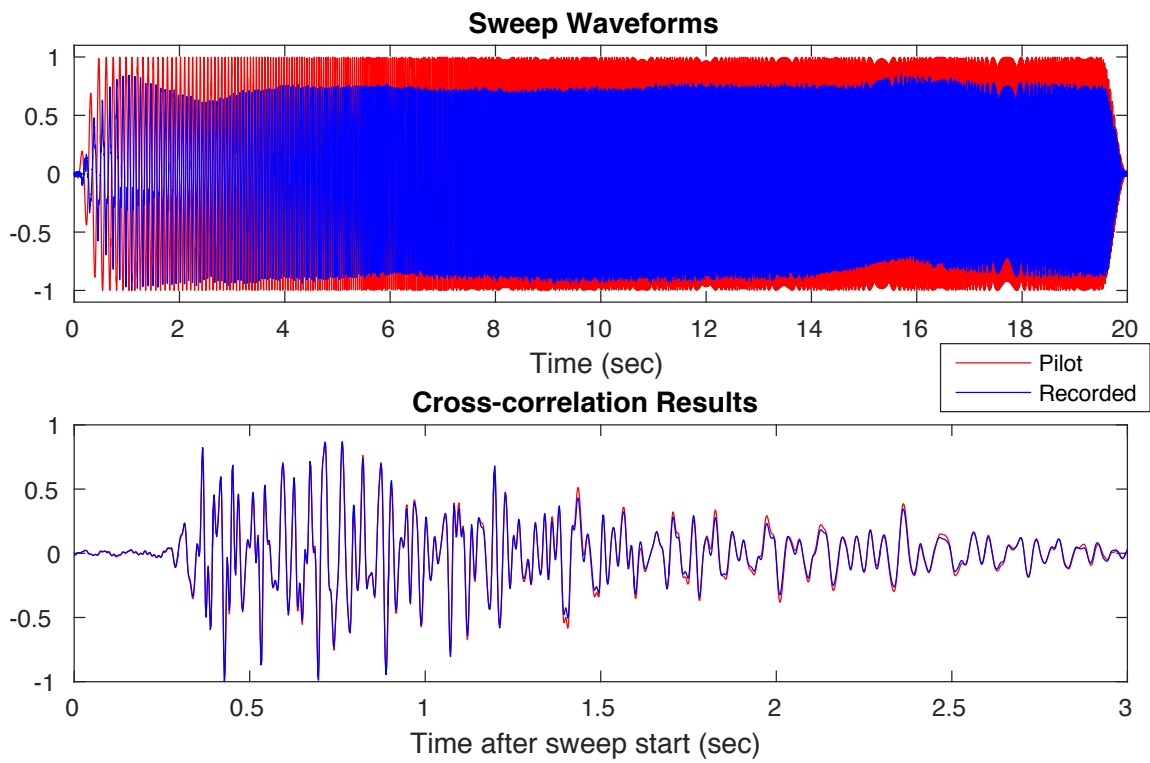


Figure 11. (Top) Difference in normalized pilot and recorded sweep waveforms. (Bottom) Normalized cross-correlation results using pilot and recorded sweep waveforms.

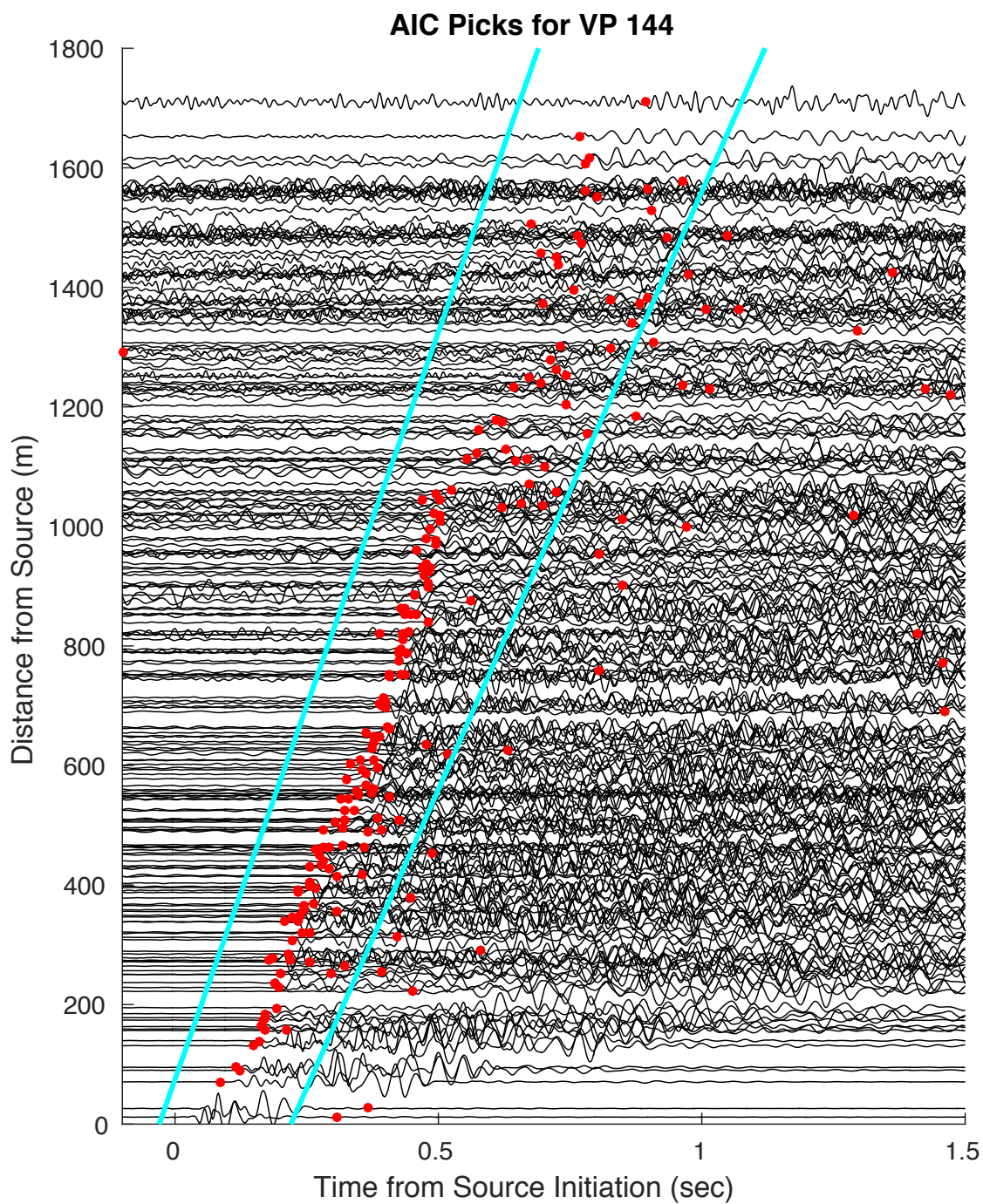


Figure 12. Unrestricted pick times from the AIC autopicker overlaid on the stacked cross-correlation waveforms plotted by distance from the source. Blue lines represent the bounds of the “acceptability” window.

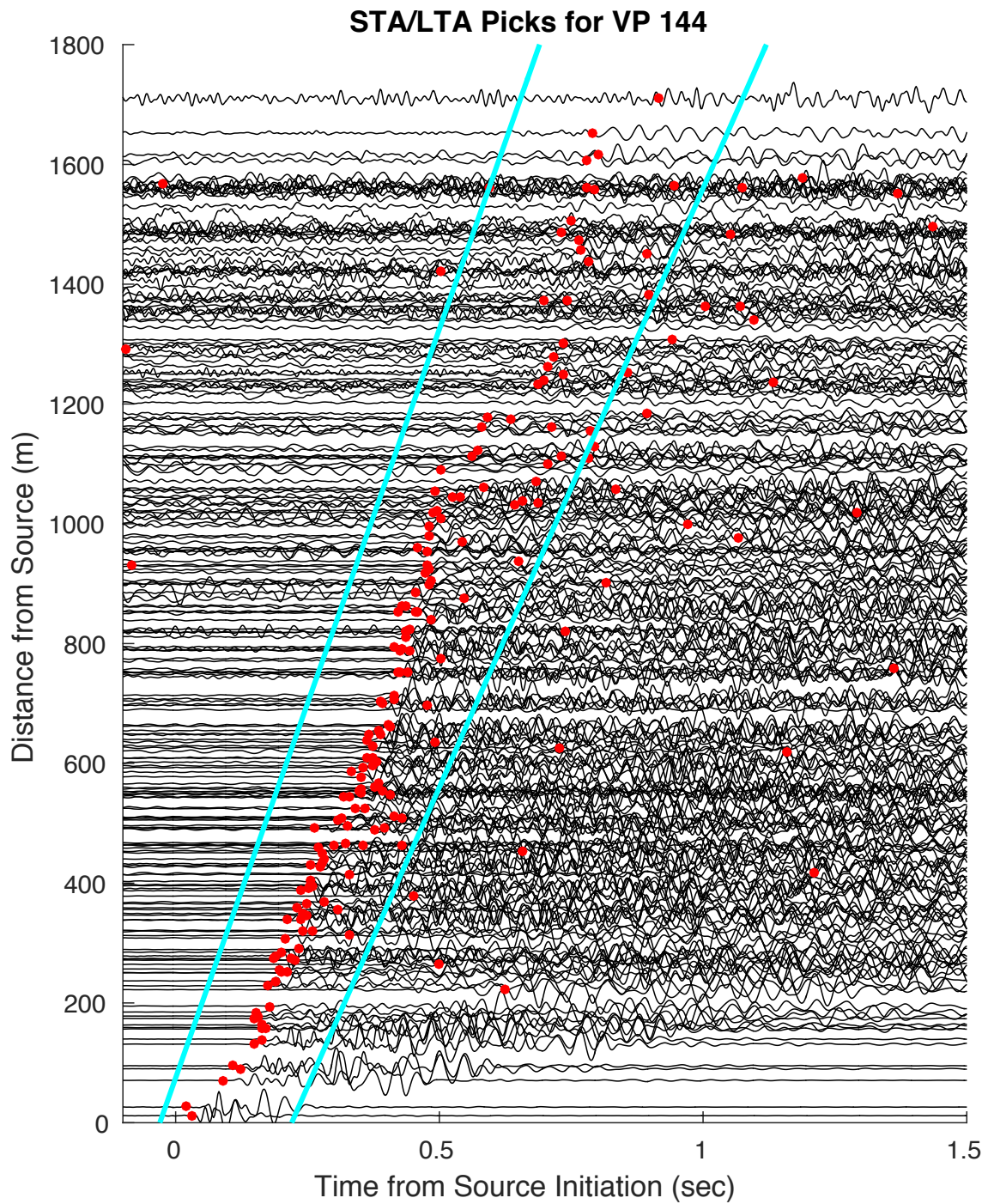


Figure 13. Unrestricted pick times from the STA/LTA autopicker overlaid on the stacked cross-correlation waveforms plotted by distance from the source. Blue lines represent the bounds of the “acceptability” window.

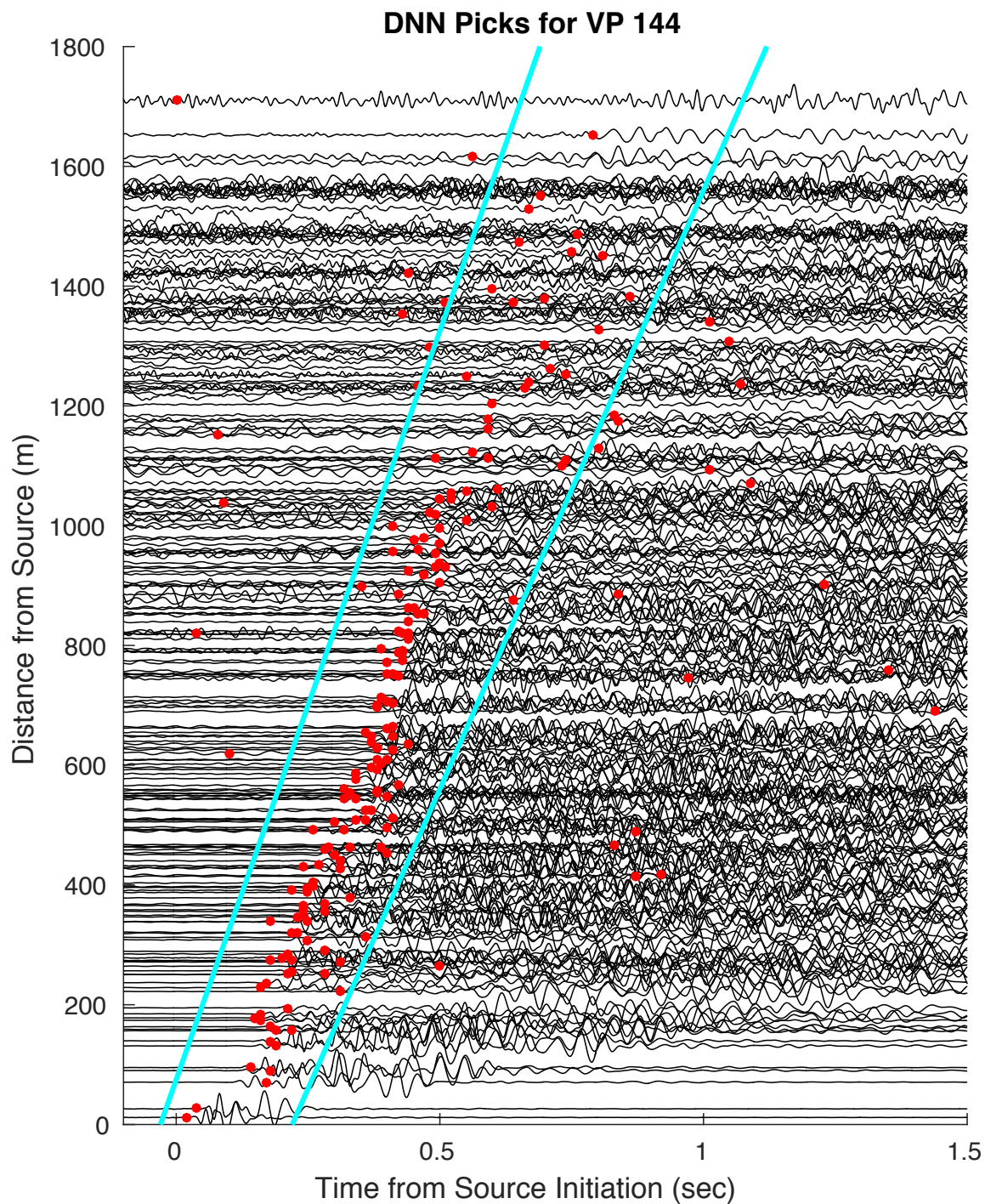


Figure 14. Unrestricted pick times from the DNN autopicker overlaid on the stacked cross-correlation waveforms plotted by distance from the source. Blue lines represent the bounds of the “acceptability” window.

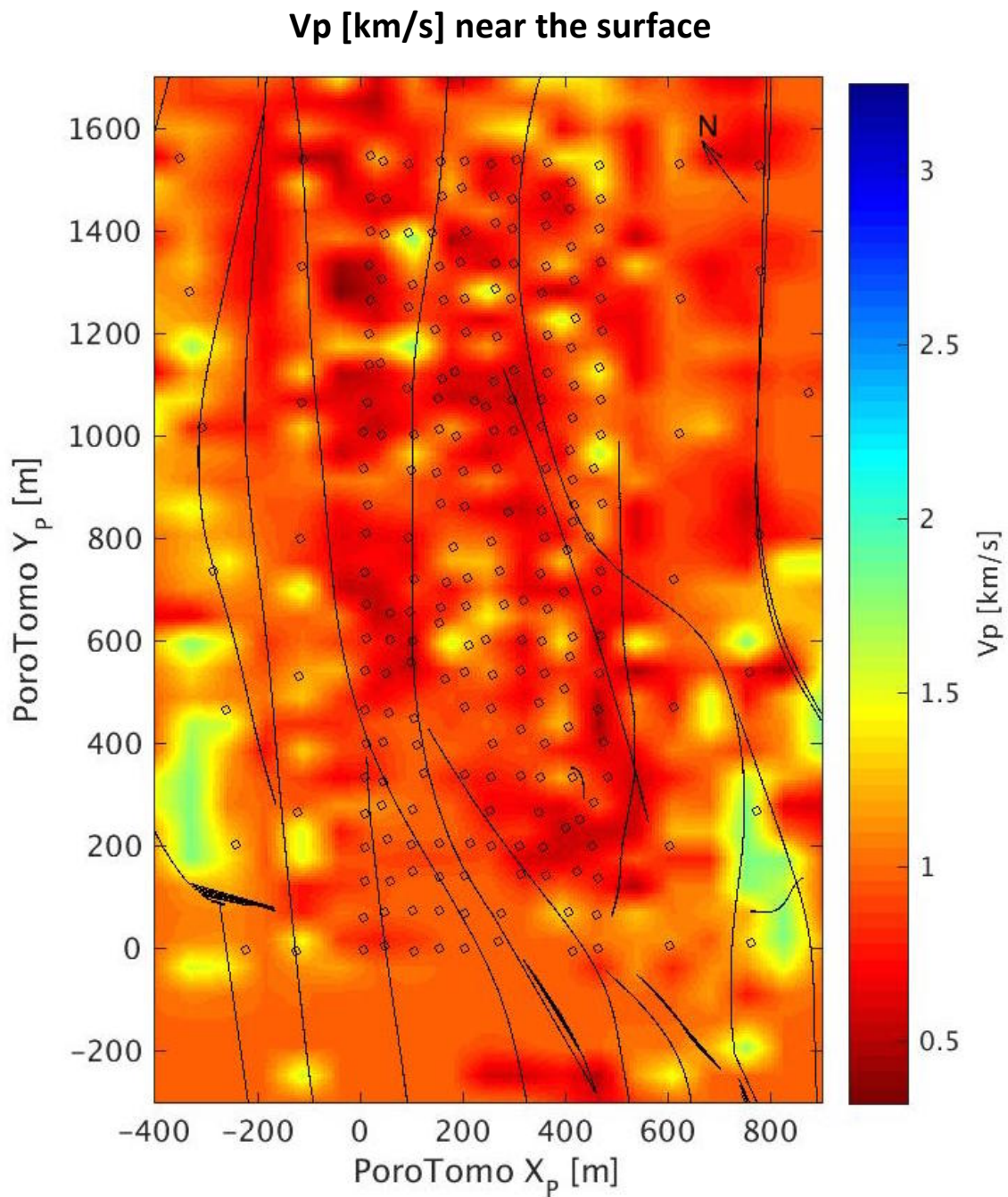
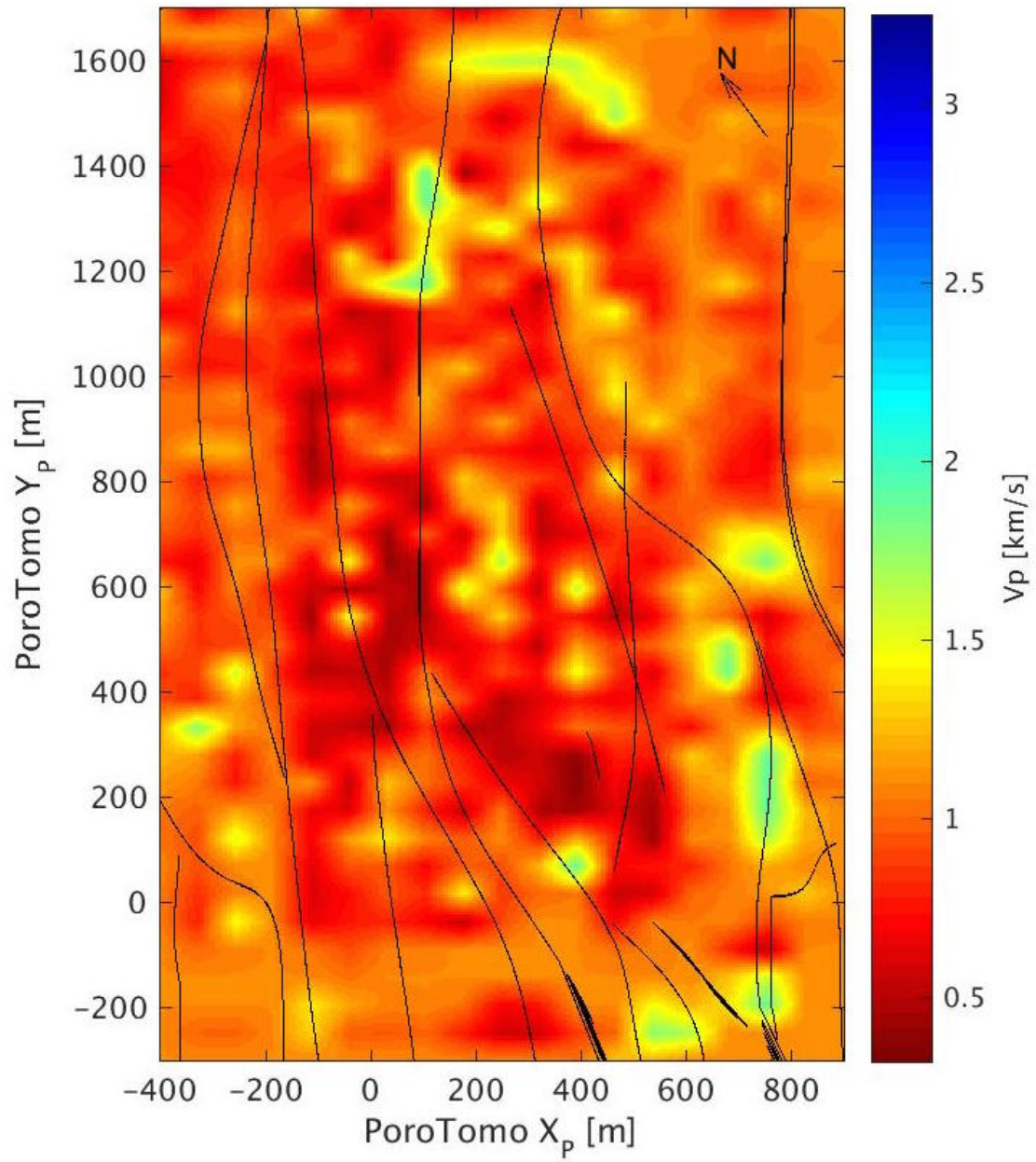
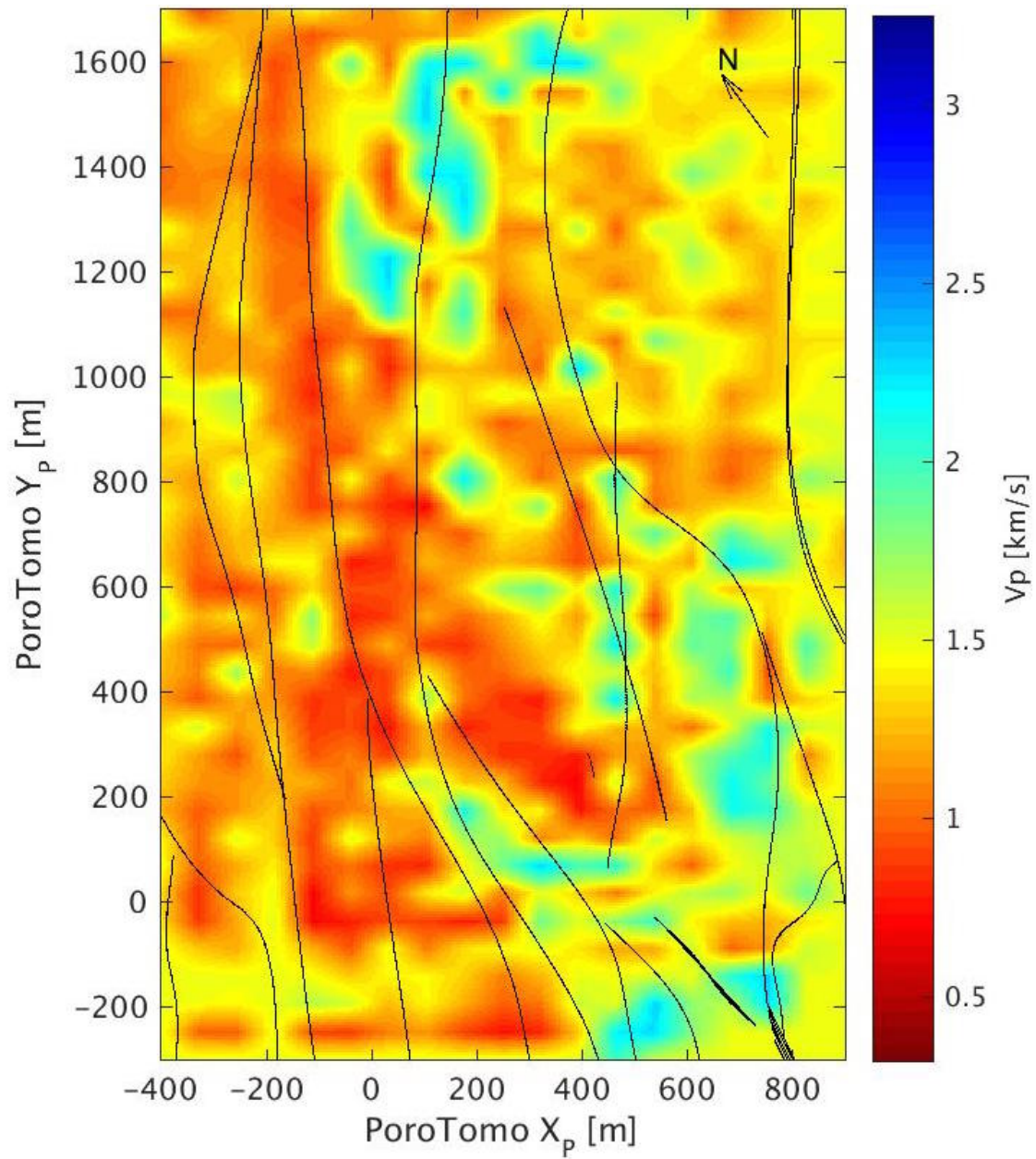
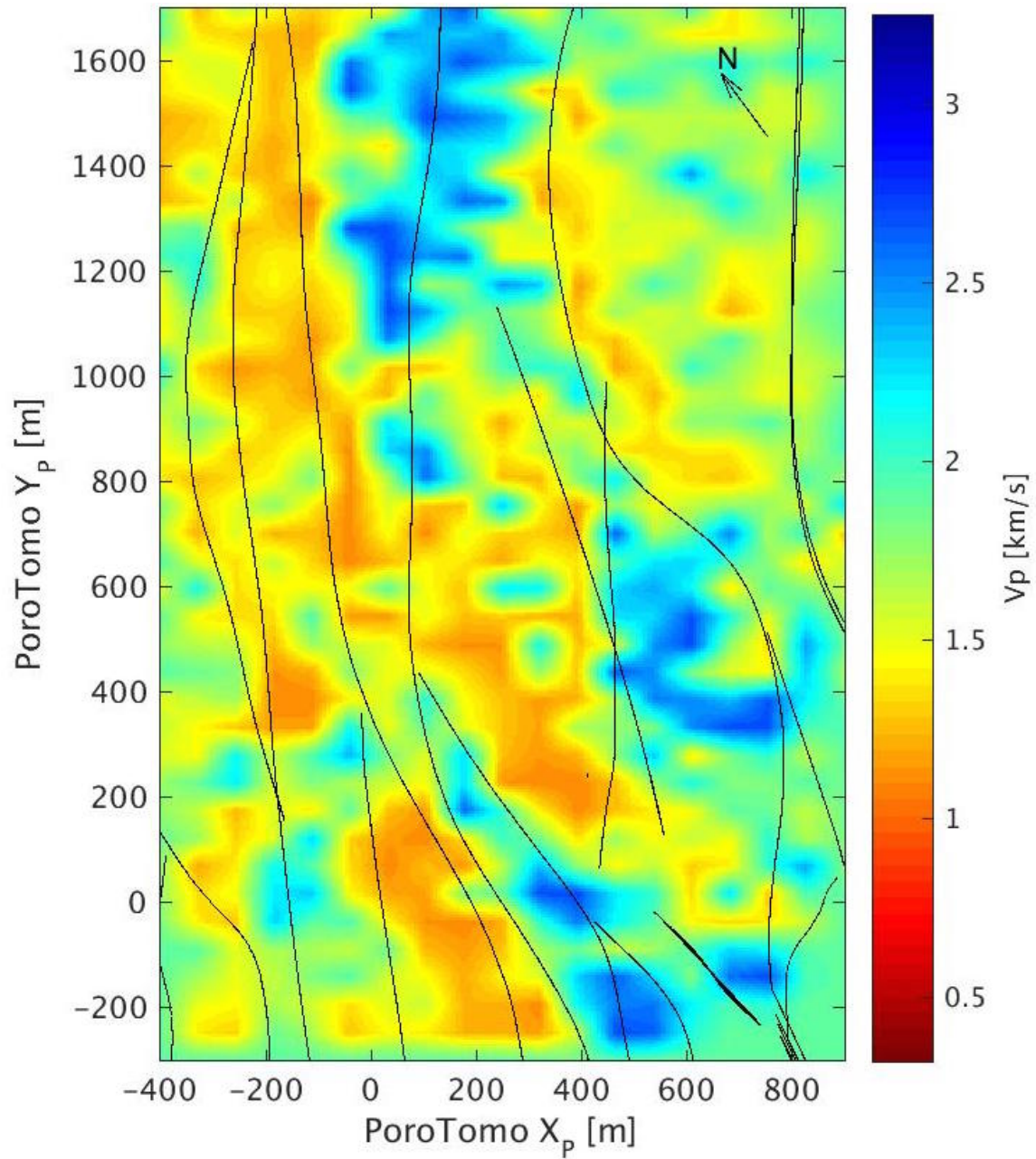
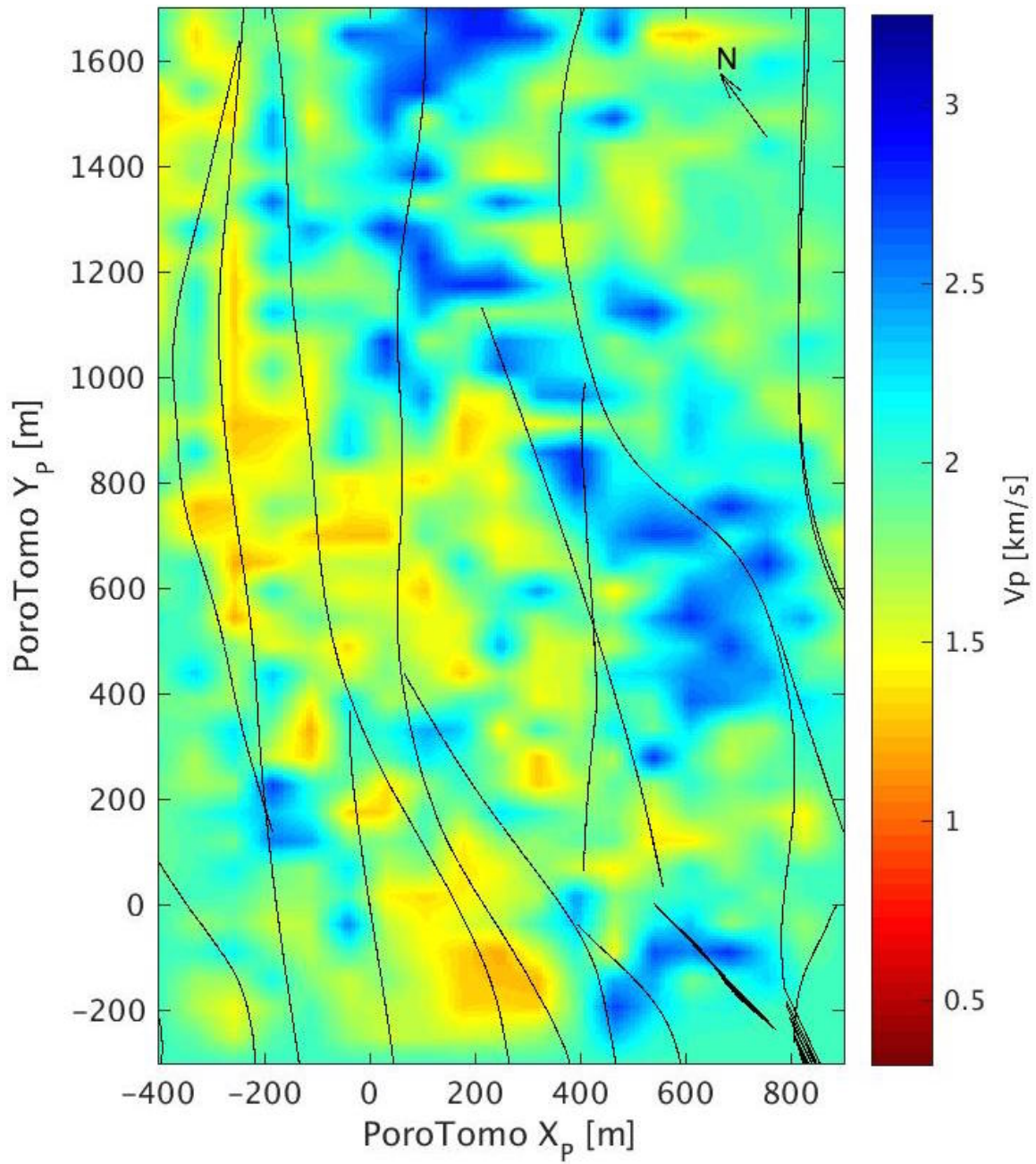


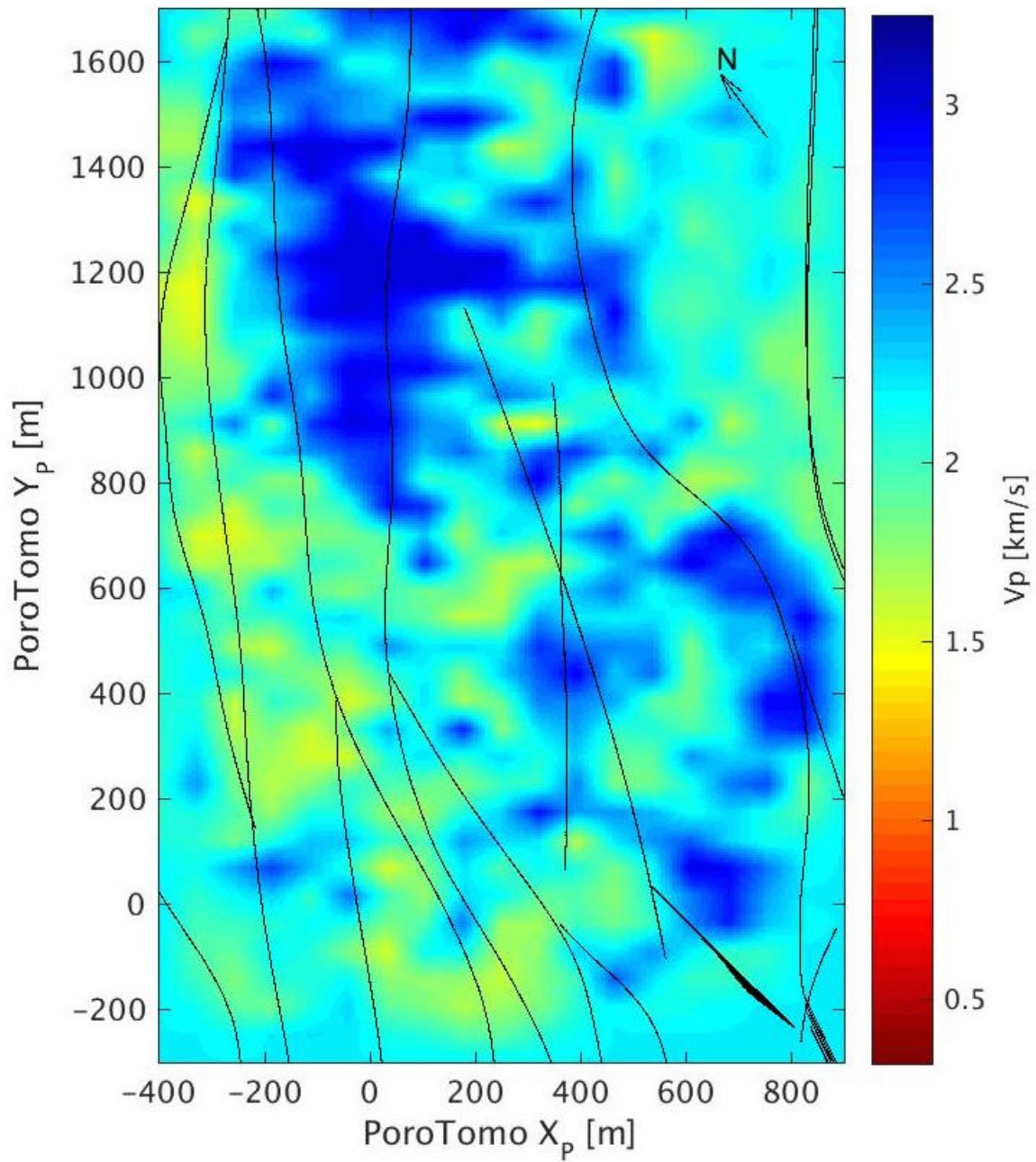
Figure 15. Stage 4 Vp model depth slices. Black circles are nodal locations. Black lines are depth projections of fault traces (Jolie, 2014; Jolie et al., 2015).

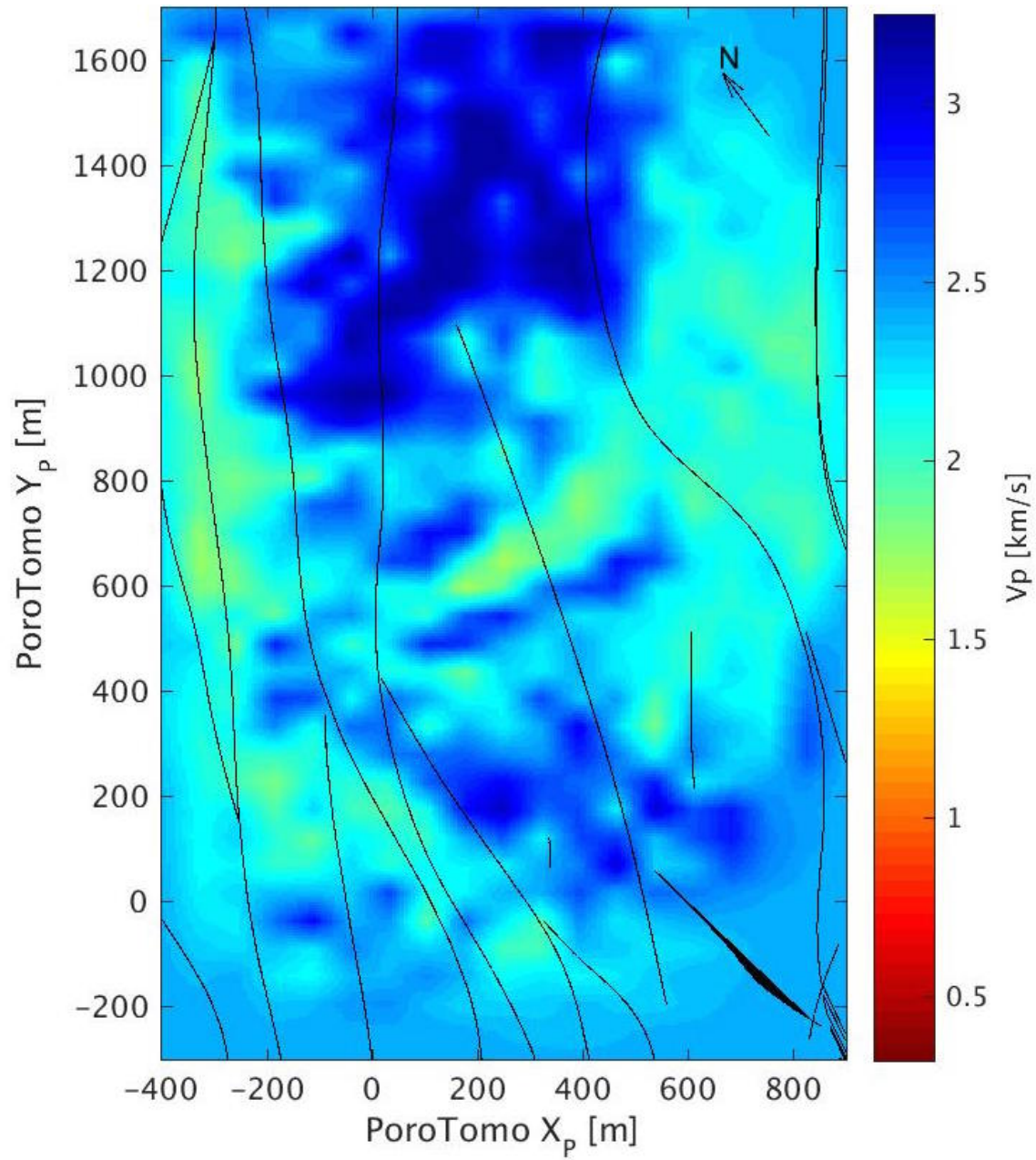
Vp [km/s] at 20 m depth

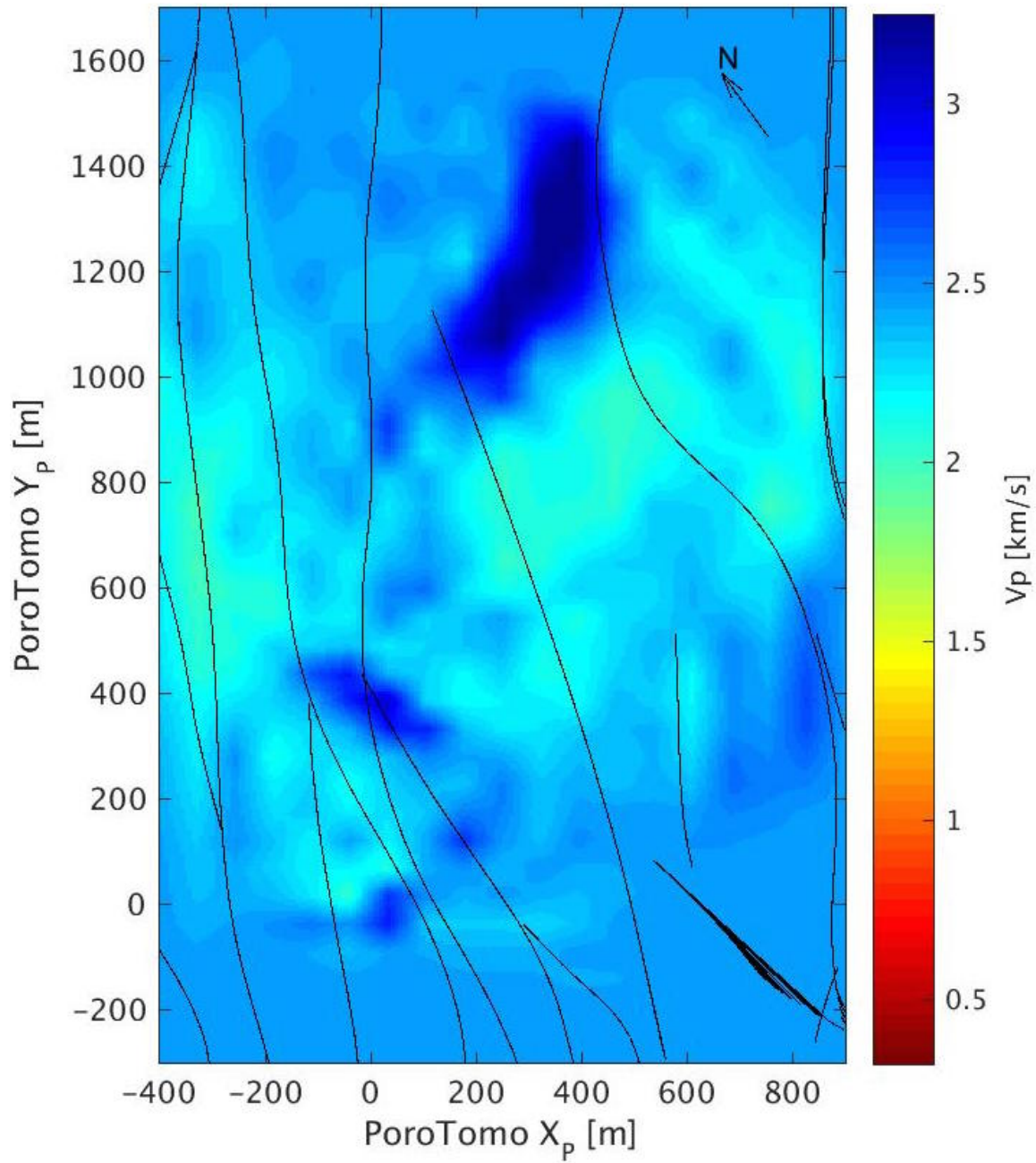
Vp [km/s] at 40 m depth

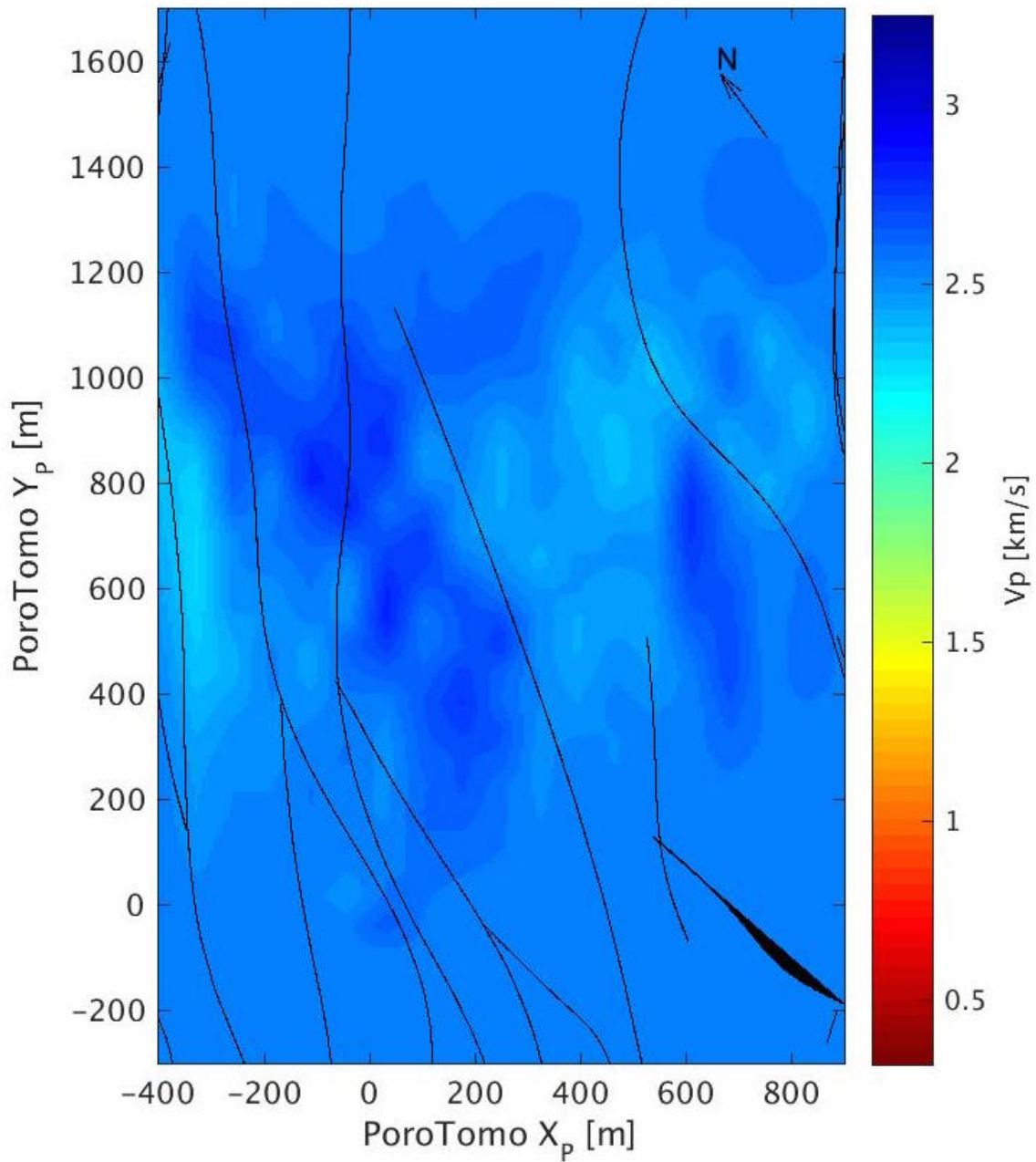
Vp [km/s] at 60 m depth

Vp [km/s] at 100 m depth

Vp [km/s] at 150 m depth

Vp [km/s] at 200 m depth

Vp [km/s] at 250 m depth

Vp [km/s] at 350 m depth

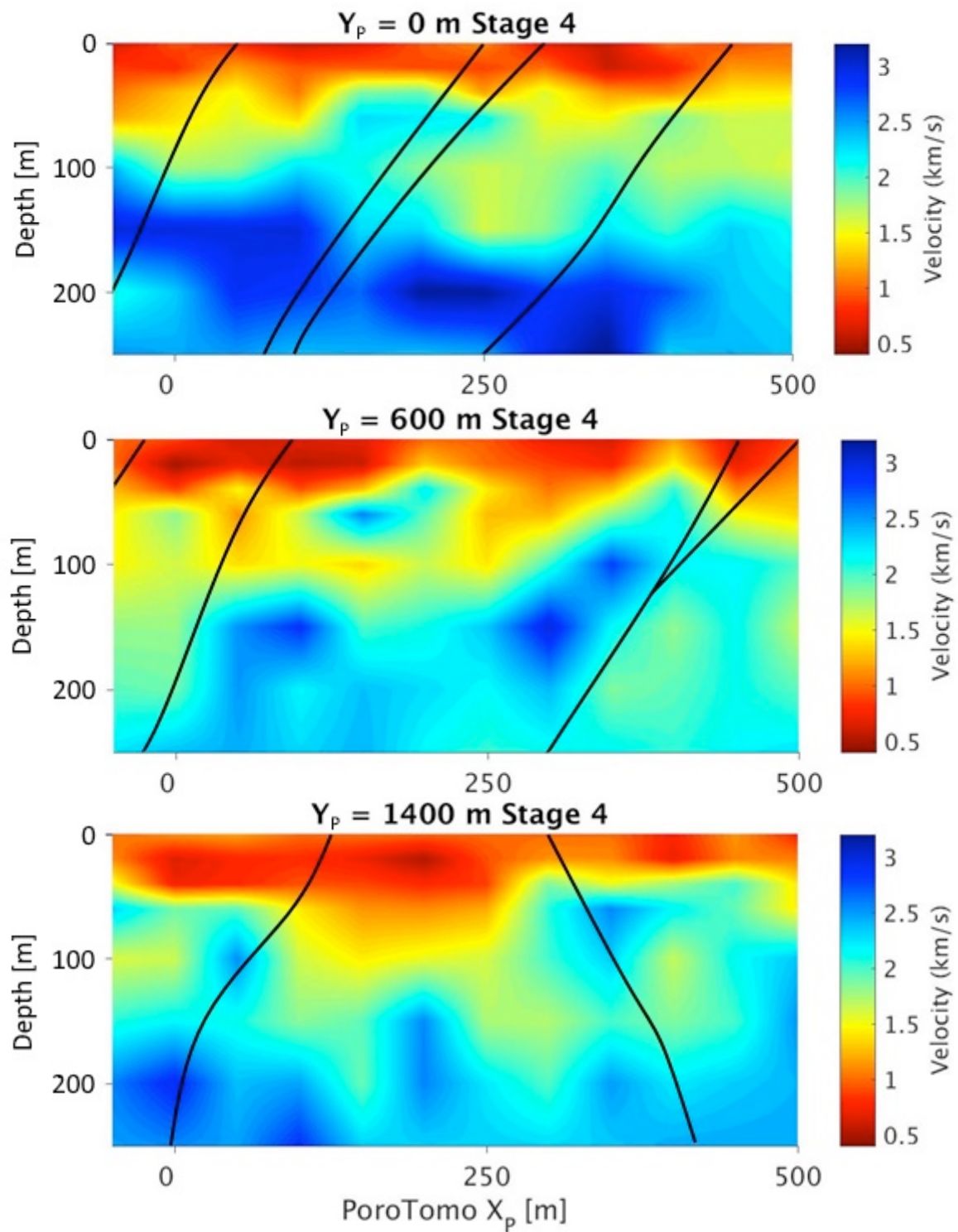


Figure 16. Cross-sections of the Stage 4 P-wave velocity model cropped to focus on the part of the model with the best resolution.

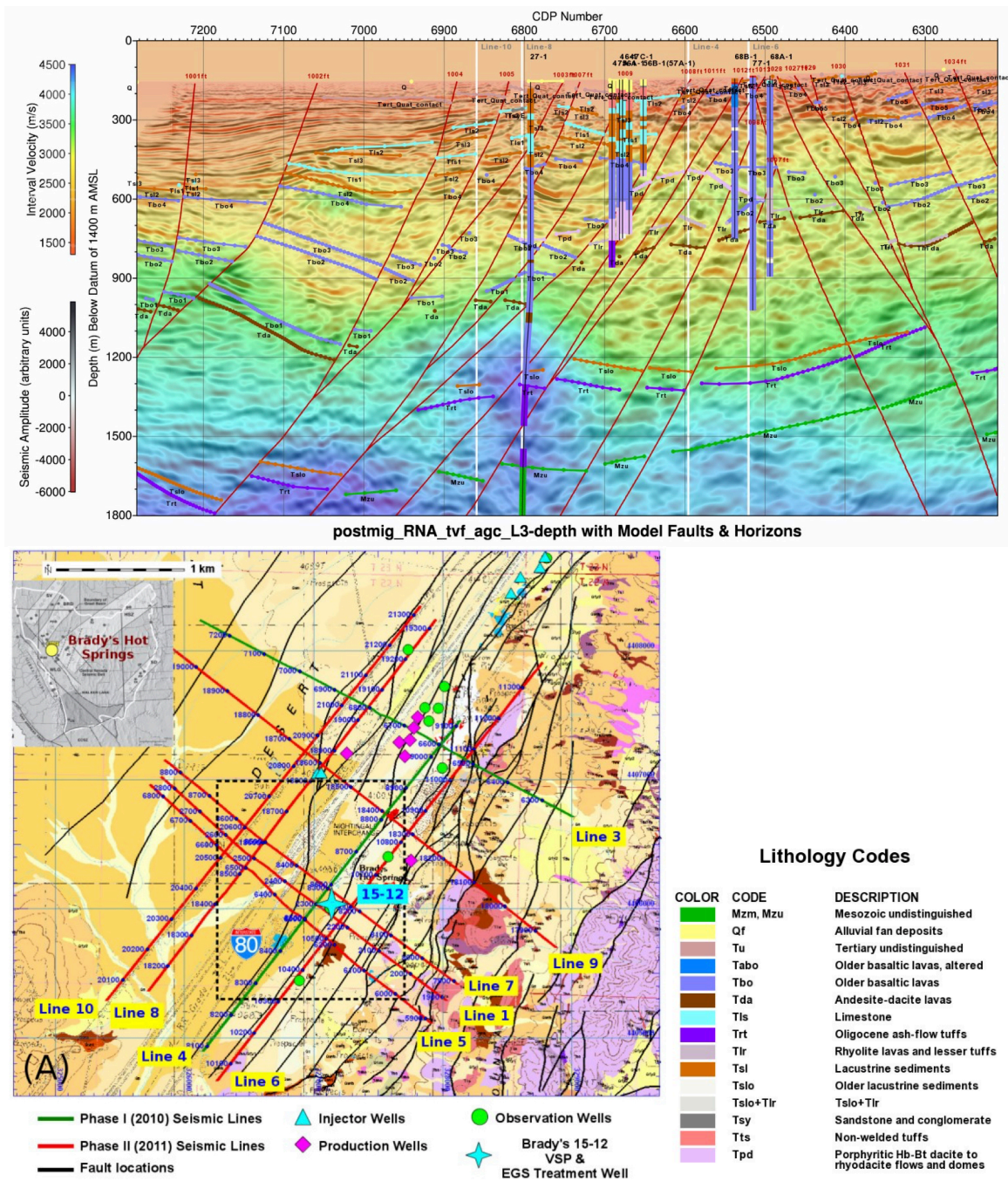


Figure 17. Line 3 post migration color-coded seismic traces overlain by color coded interval velocities, well lithologies, and 3D geological model horizon and fault picks (Queen et al., 2016).

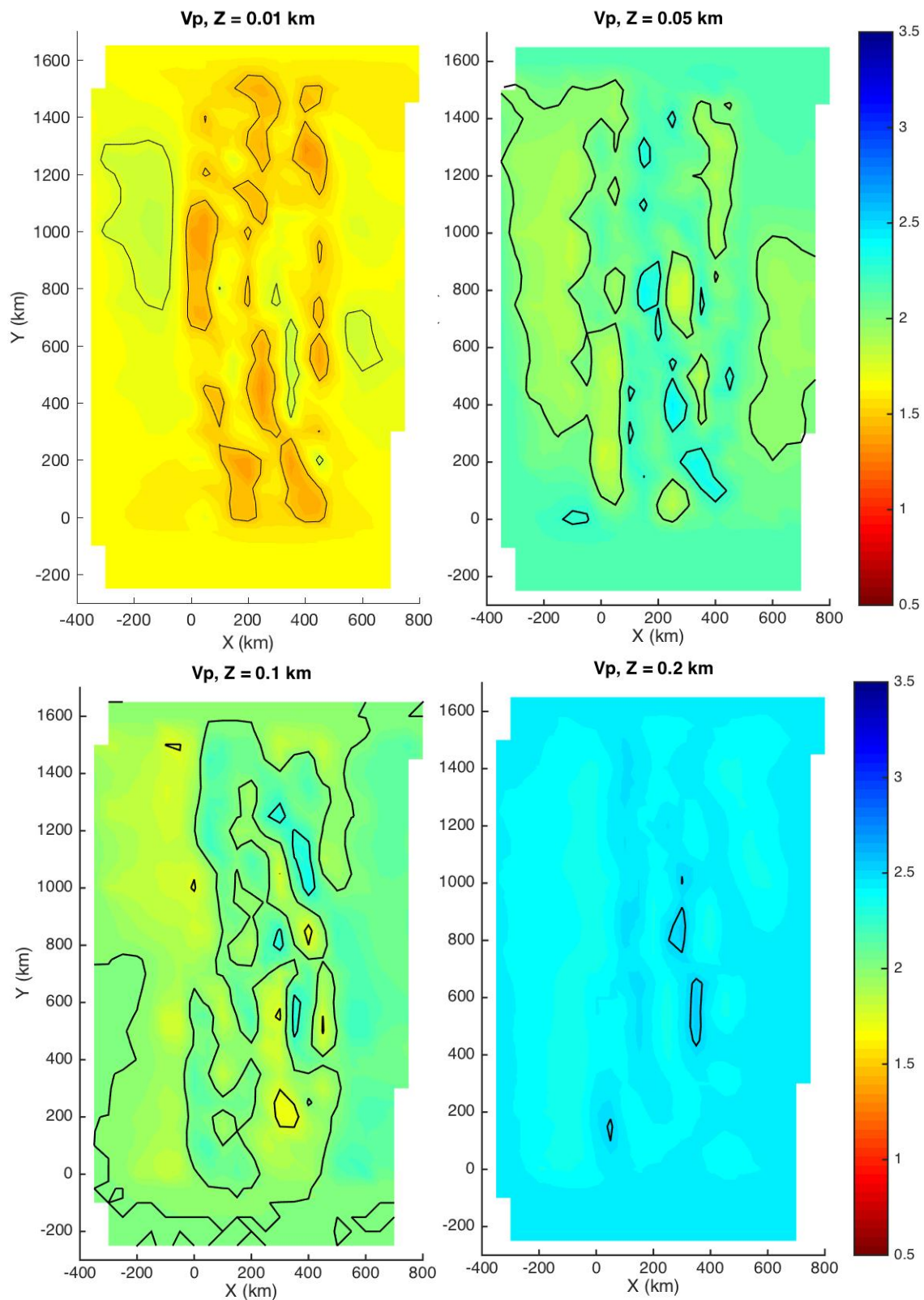
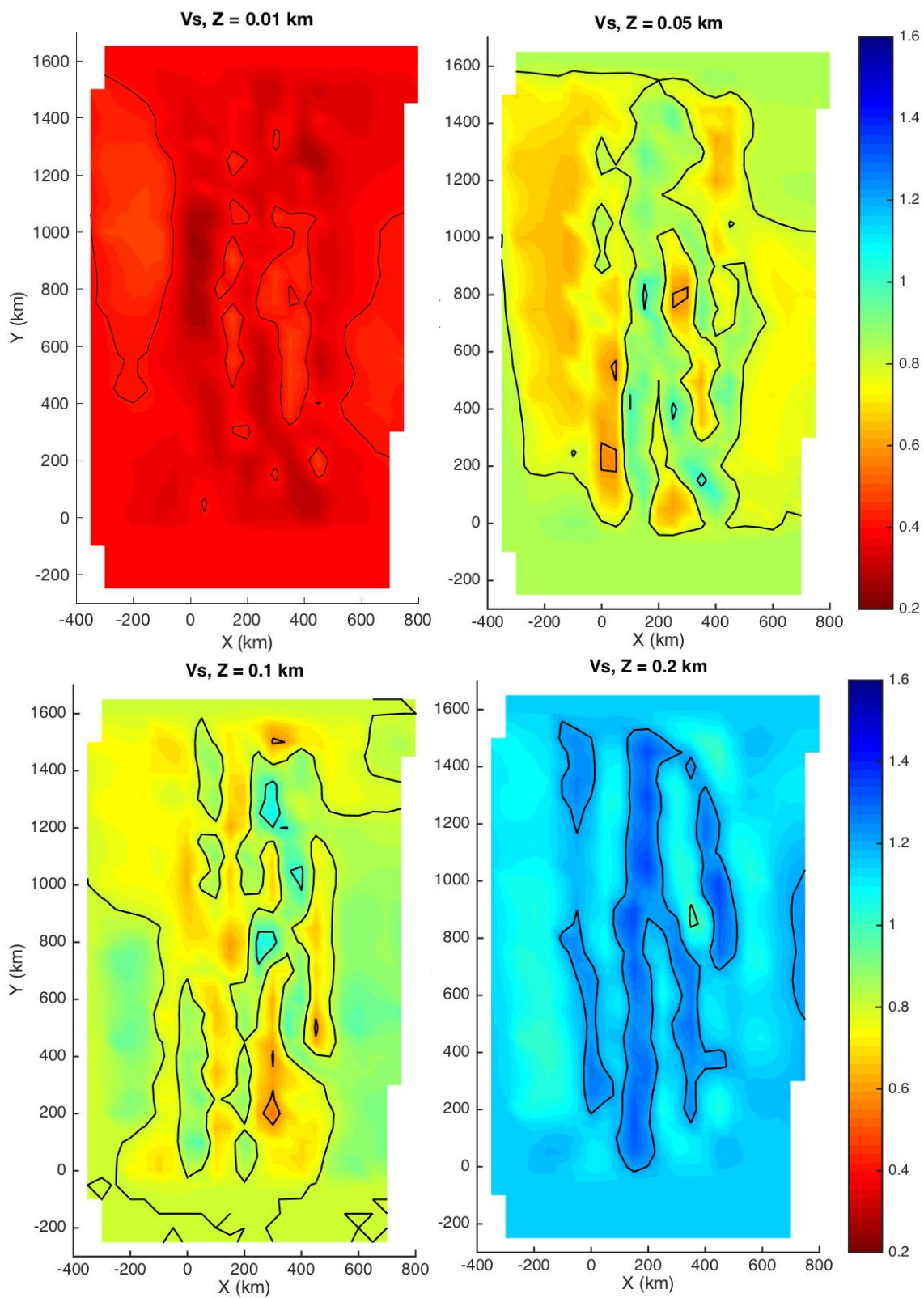


Figure 18. Depth slices for V_p and V_s ambient noise tomography models. Z is the depth from the surface. (Eric Matzel, personal communication, March 2017)



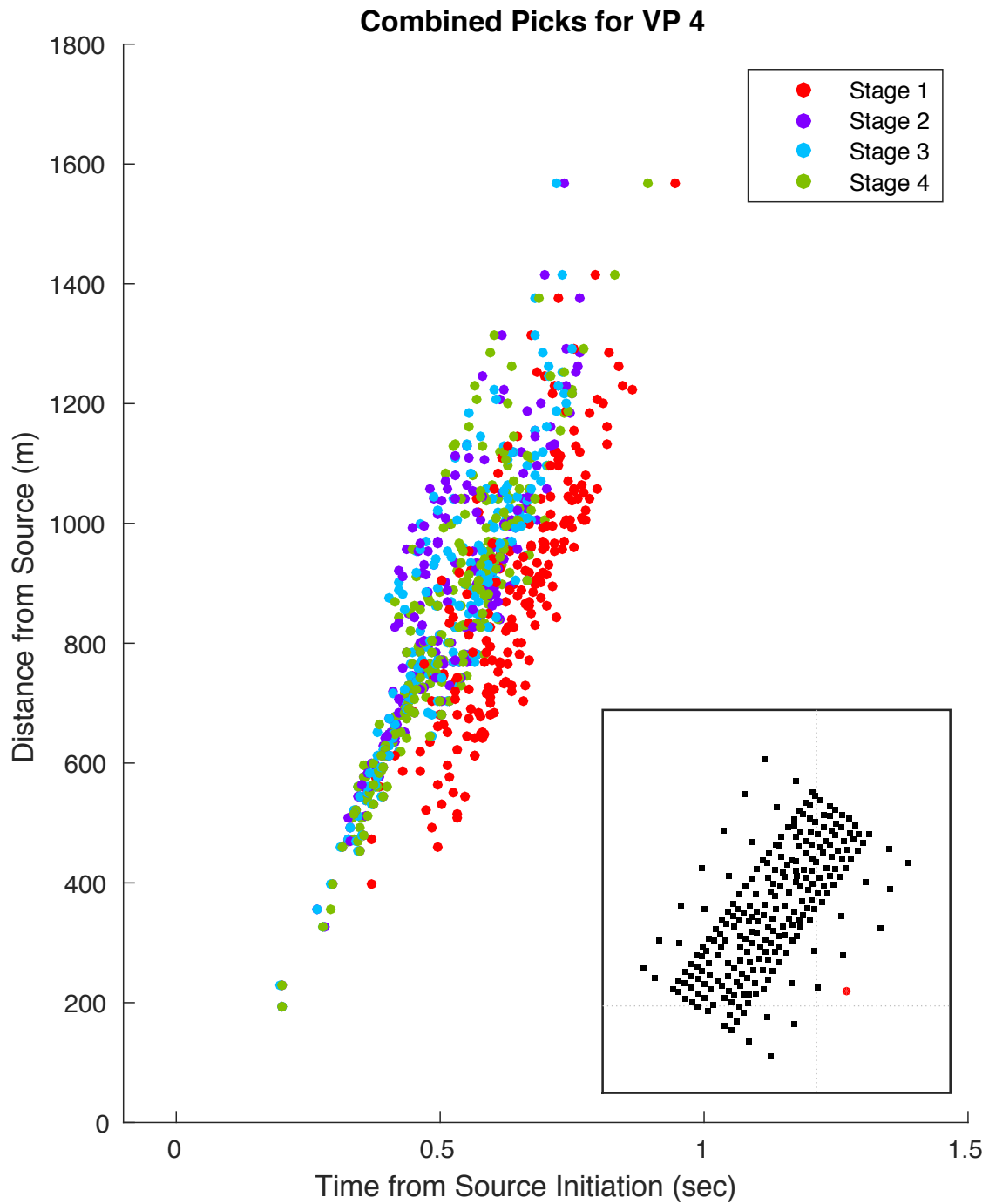


Figure 19. Arrival time plotted versus distance for all four stages of the experiment. Source location for each plot is indicated by the red dot in the inset along with the locations of each nodal instrument as black dots.

